Applied Surface Science 570 (2021) 151013

Contents lists available at ScienceDirect

Applied Surface Science

journal homepage: www.elsevier.com/locate/apsusc

Full Length Article

A combined molecular dynamics/Monte Carlo simulation of Cu thin film growth on TiN substrates: Illustration of growth mechanisms and comparison with experiments

Reza Namakian [a], Brian R. Novak [a], Xiaoman Zhang [a], Wen Jin Meng [a], Dorel Moldovan [a,b,*]

[a] Department of Mechanical & Industrial Engineering at Louisiana State University, Baton Rouge, LA 70803, United States
[b] Center for Computation and Technology, Louisiana State University, Baton Rouge, LA 70803, United States

ARTICLE INFO

Keywords:
Molecular dynamics/Monte Carlo
DC magnetron sputter deposition
Twinning
Nishiyama-Wasserman
Misfit dislocation network

ABSTRACT

Using a sequential molecular dynamics (MD)/time-stamped force-bias Monte Carlo (tfMC) algorithm to simulate the deposition of Cu species onto a TiN(001) substrate at 600 K, it is shown for the first time that at the very early stage of growth, BCC-Cu grows pseudomorphically on the TiN(001) substrate as a very thin continuous film with the BCC-Cu[001]//TiN[001] growth direction. By increasing the thickness of the Cu thin film, however, the film transforms through the Nishiyama-Wasserman mechanism from BCC into predominantly FCC-Cu with abundant nanotwins, which is the same type of structure obtained in the experiment conducted here via a dc magnetron sputter deposition technique to grow Cu on TiN(001) at 105 °C. In agreement with the experimental observations in the literature, the devised MD/tfMC is employed further to reveal that on the N-terminated TiN(111), Cu shows a very poor wettability, and FCC-Cu(111) grows vertically in the form of tall 3D islands. On Ti-terminated TiN(111) surface, however, FCC-Cu(111) initially grows in the form of 2D islands with high wettability. With additional Cu deposition, a triangular misfit dislocation network is generated at the Cu(111)//Ti-terminated TiN(111) interface with subsequent formation of a two-layer nanotwin with its twinning plane parallel to the surface substrate.

1. Introduction

Ceramic/metal interfaces are important for wide ranging engineering applications, including ferroelectric devices [1], solid oxide fuel cells (SOFC) [2], ceramic enhanced bearing systems [3], and thermal barrier coatings [4]. The electrical or mechanical response of ceramic/metal interfaces can be critical for the performance of the entire engineering system. One main approach for synthesizing specimens containing ceramic/metal interfaces is through various vapor phase thin film growth techniques. Metal or ceramic thin films deposited onto polycrystalline or amorphous substrates tend to be polycrystalline. The structure of such polycrystalline/polycrystalline, and often nanocrystalline/nanocrystalline, interfaces are complex, raising difficulties for interpretation of electrical or mechanical response data obtained from such interfaces. It is thus desirable to synthesize ceramic/metal interfaces with better-defined structures. One primary means for preparing ceramic/metal interfaces with well-defined structures is through ultra-high-vacuum (UHV) vapor phase epitaxial growth. Vapor phase epitaxy of Si, GaAs, and related materials provides the foundation of modern electronic and optoelectronic devices, and embodies in so doing basic concepts about bi-material interfaces such as coherency, semi-coherency, misfit dislocations, and energetics of misfit accommodation [5]. Epitaxial growth of thin films of engineering ceramics, due to their refractory nature, often invokes growth assist by energetic particle bombardment to promote surface mobility and improve film quality, as manifested in various forms of ion-beam- or plasma- assisted deposition techniques [6].

MgO single crystals, with a B1 (NaCl) structure and a bulk lattice parameter $a_{MgO} = 4.21$ Å is a popular substrate for epitaxial growth of engineering ceramics, such as transition metal nitrides and carbides [7]. Prototypical transition metal mono-carbides and -nitrides, such as TiC and TiN, also possess the B1 structure with lattice parameters matching that of MgO, $a_{TiC} = 4.33$ Å [8] and $a_{TiN} = 4.24$ Å [9]. Epitaxial growths of TiC and TiN have both been achieved on MgO(001) [10,11]. Interface between elemental metals and B1 structured ceramics have served as model systems for studying ceramic/metal interfaces, an example of which is the Cu/MgO interface [12]. With an FCC crystal structure and a bulk lattice parameter of $a_{Cu} = 3.61$ Å, the Cu/MgO system possesses a

* Corresponding author at: Department of Mechanical & Industrial Engineering at Louisiana State University, Baton Rouge, LA 70803, United States.
E-mail address: dmoldo1@lsu.edu (D. Moldovan).

https://doi.org/10.1016/j.apsusc.2021.151013
Received 26 June 2021; Received in revised form 9 August 2021; Accepted 17 August 2021
Available online 25 August 2021
0169-4332/

large lattice mismatch, $(a_{Cu} - a_{MgO})/a_{MgO} = -0.1425$. Nonetheless, heteroepitaxial growth of Cu thin films on MgO substrates have been achieved by UHV vapor phase growth [13,14]. Epitaxial TiN(001) thin films grown on MgO(001) have also been used as a growth template for growth of Cu thin films [15].

The orientation relationship (OR) between epitaxial Cu films grown on MgO substrates and TiN thin film templates grown on MgO substrates is usually reported to be "cube-on-cube", with Cu(001)//MgO(001) and Cu[100]//MgO[100] or Cu(001)//TiN(001) and Cu[100]//TiN[100] [13–15], henceforth denoted by OR_A. In a recent paper, the present authors have demonstrated a new OR between Cu and TiN. TiN(001) thin films were grown heteroepitaxially on MgO(001) substrates in the "cube-on-cube" orientation and used as templates for growth of Cu thin films. While the Cu/TiN "cube-on-cube" OR was demonstrated at a Cu film growth temperature of ~75 °C, a new Cu/TiN OR resulted from a slight increase in the growth temperature to ~105 °C: Cu(110)//TiN (001) in the growth direction and Cu⟨111⟩//TiN⟨100⟩ and Cu⟨112⟩// TiN⟨100⟩ within the growth plane [16], henceforth denoted by OR_B. While post-growth structural characterization of Cu films grown onto TiN(001)/MgO(001) templates has shown unequivocally the new Cu/TiN OR_B, it does not provide clues to the mechanisms responsible for the puzzling observation that, with a mere ~30 °C increase in growth temperature, two significantly different ORs would manifest in the same Cu-TiN system.

Atomistic simulations, such as density functional theory (DFT), molecular dynamics (MD), and Monte Carlo (MC), have been shown to be invaluable tools to provide atomic scale understanding of thin film structures and to obtain results on interfacial energetics [17,18], interfacial defect configurations [19], interfacial or material response to mechanical stresses [20–22], and kinetic processes at surfaces and interfaces. With appropriate experimental calibration and validation, such physics-based simulations provide additional insights into physical mechanisms difficult to ascertain with experimentation alone. MD simulations are often limited by the availability of relevant potentials. In the case of Cu/TiN system, modified embedded atom method (MEAM) potentials have recently been developed, enabling MD simulations to be performed [23].

Deposition of atoms onto a substrate involves fast events which usually are resolved by employing simulation methodologies characterized by fine temporal resolution, such as MD [24]. To accurately resolve the fastest modes of motion and maintain simulation stability, the timestep should be chosen sufficiently small (~1 fs for example). Thus, MD simulations rarely reach timescales beyond hundreds of nanoseconds, depending on the size of the simulation system and the interatomic potential. As such, MD simulations cannot capture slower yet important relaxation events that play an important role in microstructure development during thin film growth. For example, it was documented that longer timescale thermal relaxation processes during vapor phase deposition are very often critical in determining the final thin film properties [24–26]. In fact, in a typical MD trajectory, it is likely that only a small subset of basins in the potential energy landscape of the system that are most quickly accessible to an initial configuration will be sampled well [27]. In contrast to MD simulations, where a single long trajectory of the system through phase space can be generated, atoms are displaced stochastically in Monte Carlo (MC) simulations, which leads to broader sampling of the phase space and often to faster thermal equilibration [24,26]. Considering the difference in timescales between the fast processes and the slower relaxation events, one strategy to simulate vapor phase thin film growth is to employ MD and MC in a cyclic or alternating fashion. According to this approach, MD is used to capture atomic impingements on a surface during deposition, and MC is employed subsequently so that thermal relaxation events with a longer characteristic timescale can be reached [24,26]. Among different MC-based approaches used in vapor phase growth simulations [24,26,28–32], the time-stamped force-bias Monte Carlo (tfMC) method has the advantage of allowing for a timescale to be associated with the simulation. Moreover, tfMC is easy to implement and has the advantage that it does not require any prior knowledge about the reactive events or energy barriers [24,26,28,29]. Because tfMC relies on deterministic forces when selecting the atomic displacements, as opposed to stochastic displacements in conventional MC methods, it ensures much larger acceptance ratios [24,26]. Recently, a hybrid MD/tfMC has been successfully applied to modelling the plasma-assisted growth processes of nanocrystalline carbon films, and it has been shown that the classic MD simulation alone was not able to simulate formation of nanocrystalline carbon structures from a totally amorphous carbon structure because of the limitation of the MD timescale [33].

In this work we taylor and calibrate a sequential MD/tfMC simulation methodology to investigate the growth mode, the resulting crystalline structure, and the orientation of Cu thin films during sputter deposition on epitaxial TiN thin film templates. Our main objective is to provide an atomistic-level understanding of the mechanism(s) of Cu thin film microstructure development during various stages of the deposition process, i.e., initial island nucleation, growth, coalescence, and overall formation of Cu film on TiN templates of different orientations. The simulation results provide critical insights into the film growth mechanisms and complexities associated with the larger class of weakly-interacting metal thin film layer on ceramic substrate systems. In what follows, Section 2 describes methodologies for both experimentations and simulations; Section 3 summarizes the major results: experimental observations followed by simulated Cu growth on TiN templates; Section 4 provides additional discussions; and Section 5 gives a summary.

2. Methodology

2.1. Experimentation

Backside Si-coated single crystal MgO(001) wafers (99.99%) were cleaned with acetone and ethanol, dried with blowing dry N_2, mounted onto a Mo holder, and inserted into an ultra-high-vacuum (UHV) dc magnetron sputter deposition chamber with a base pressure below 1×10^{-9} Torr. The deposition chamber houses two 7.5 cm diameter Ti (99.95%) magnetron sputter sources, one 7.5 cm diameter Cu (99.99%) magnetron sputter source, and a high temperature substrate heating stage. The actual substrate temperature was determined through infrared optical pyrometry, cross referenced to a separate thermocouple placed in close proximity to the Mo holder. The MgO(001) wafers were thermally degassed in UHV at 800 °C for 20 min. Reactive sputter deposition of TiN onto the MgO(001) substrate commenced immediately after degassing at the same temperature, with the Ti sputter sources operated in the dc mode at 1.35 A in an Ar/N_2 (99.999%) mixture at a total pressure of ~4 mTorr. During TiN deposition, a −40 V substrate bias voltage was applied. Input N_2 flow was adjusted for stoichiometric deposition. After the TiN deposition, the substrate temperature was equilibrated at the desired Cu deposition temperature, and sputter deposition of Cu commenced in pure Ar (99.999%) at a total pressure of ~4 mTorr, with no substrate bias voltage applied. After Cu deposition, the Cu/TiN/MgO(001) specimen was cooled to room temperature before removal from the deposition system. Cu/TiN/MgO(001) specimens were made at varying Cu layer growth temperatures and layer thicknesses, keeping the growth temperature of the TiN buffer layer fixed at 800 °C. Additional details on film deposition were described previously [16].

The morphology and structure of Cu/TiN/MgO(001) specimens were characterized by scanning electron microscopy and Ga^+ focused ion beam sectioning (SEM/FIB), X-ray diffraction (XRD), and transmission electron microscopy (TEM). Scanning imaging with electron- or ion-induced secondary electrons (SEs/ISEs) and Ga^+ FIB milling were carried out on an FEI Quanta3D Dual-Beam FEG instrument with an X-ray energy dispersive spectroscopy (EDS) attachment (EDAX), a Ga^+ ion beam catalyzed organometallic Pt deposition attachment, and an OmniProbe attachment for site-selective specimen lift-out. X-ray

symmetric θ/2θ scans, asymmetric ϕ scans, ω rocking curve scans, and reciprocal lattice mapping (RSM) were collected on a PANalytical Empyrean system [16]. A JEOL JEM2011 microscope operated at 200 kV was used for electron selected area diffraction (SAD) as well as bright-field/dark-field (BF/DF) imaging. TEM specimen preparation proceeded with OmniProbe lift-out, Ga^+ ion milling in the SEM/FIB instrument, and finished with low energy Ar^+ ion polishing at 100 eV with a Gatan precision ion polishing system (PIPS-II).

2.2. General simulation methodology

All simulations were performed by using the Large-scale Atomic/Molecular Massively Parallel Simulator (LAMMPS) [34] package. The interactions between atoms were modeled by using a recently developed modified embedded atom method (MEAM) potential for the Cu-TiN system [23].

The pristine TiN substrate supercells were constructed using Atomsk [35]. The energy minimization of the initial simulation structures was performed in two steps by first employing the Polak-Ribiere version of the conjugate gradient algorithm followed by the damped dynamics method of fast inertial relaxation engine (FIRE) [36]. The stopping tolerance values for energies and forces were 10^{-3} meV and 10^{-3} meV/Å, respectively, for both energy minimization procedures.

Following is the methodology for all MD simulations except for the Cu melting point calculation discussed below. A standard velocity-Verlet integrator was used. To ensure an optimized balance between the computational efficiency and accuracy, the timestep was increased or decreased subject to the constraint that no atom in the system traveled a distance greater than 0.01 Å, following the criterion suggested in [28]. Approaching the target temperature of 600 K in the current Cu deposition simulations was done using a Langevin thermostat [37] where the time-discretization of the Langevin model in [38] is followed, and the time constant or damping parameter was set to be one thousand times the integration timestep used. Also, the drift due to randomly and independently generated forces by using this thermostat on different atoms was eliminated. To update the positions and velocities of atoms sampled from the canonical (NVT) ensemble (or isothermal-isobaric (NPT) ensemble) [39–42], thermostatting (and barostatting) in the MD simulations was performed according to the following procedure. To ensure that the desired temperature (and pressure) reached a steady value in an average sense in the region of interest, the time integration was performed on the Nose-Hoover style non-Hamiltonian equations of motion each timestep to update the positions and velocities for atoms in the NVT (or NPT) ensemble. For the Nose-Hoover thermostat and Nose-Hoover barostat, the time constants for temperature and pressure relaxation toward the desired values were set to be 100 and 1000 times the timestep, respectively. To control initial oscillations in temperature and pressure, chains of thermostats and barostats with five links were employed. Furthermore, to improve the accuracy of the integration scheme, the initial and final updates of the thermostat and barostat variables were discretized into one hundred sub-steps [42]. In addition, for the NPT integrator, the reference dimensions were reset every 1000 steps to allow for the final average pressure tensor to converge smoothly to the specified values of the external stress tensor. Also, to control the true Cauchy stress during NPT integration, the proportional gain parameter α was set to 0.001 [43].

The tfMC algorithm is essentially a variant of the uniform-acceptance force-biased Monte Carlo algorithm that was developed to increase the acceptance probability of atomic displacements in strongly interacting systems, thus allowing faster evolution to equilibrium. The significantly higher acceptance ratios, compared to classical Metropolis Monte Carlo (MMC) algorithm, is achieved by including the effect of deterministic forces acting on atoms into the stochastic algorithm. That is, in the tfMC approach, at each MC step, possible displacement of each atom is not chosen randomly inside the designated displacement domain $D(\boldsymbol{r})$ but is instead dependent on the forces acting on it. Thus, the effect of force biasing the atomic displacements is that the displacements in the direction of the forces acting on atoms are more probable than those in directions against these forces. Therefore, the tfMC approach bears some similarity to MD, and it is even possible, under certain conditions, to assign a time scale to the tfMC simulations.

As detailed in [26], the main ingredient of the tfMC algorithm is the definition of the methodology used to calculate the location of the atoms in space, as a result of one iteration. Specifically, assuming that all atoms are of the same type, in a single tfMC step, each atom i is displaced from its initial position $\mathbf{r}_i$ to the final position $\mathbf{r}_i^* = \mathbf{r}_i + \boldsymbol{\xi}_i\Delta$, with Δ corresponding to the maximum displacement from the initial position and $\boldsymbol{\xi}_i = (\xi_{i,1}, \xi_{i,2}, \xi_{i,3})$, where each component, $\xi_{i,j}$, with $j = 1,2,3$ takes value in $[-1,1]$, is a stochastic variable distributed according to the probability distribution function given by

$$p(\xi_{i,j}) = \begin{cases} \dfrac{e^{\gamma_{i,j}(2\xi_{i,j}+1)} - e^{-\gamma_{i,j}}}{e^{\gamma_{i,j}} - e^{-\gamma_{i,j}}} & , \quad if \quad \xi_{i,j} \in [-1,\ 0[\\ \\ \dfrac{e^{\gamma_{i,j}} - e^{\gamma_{i,j}(2\xi_{i,j}-1)}}{e^{\gamma_{i,j}} - e^{-\gamma_{i,j}}} & , \quad if \quad \xi_{i,j} \in]\ 0,\ 1] \end{cases}, \tag{1}$$

with

$$\gamma_{i,j} = \frac{F_{i,j}\Delta}{2k_BT}, \tag{2}$$

where $F_{i,j}$ is the force on atom i along the direction j, k_B is the Boltzmann constant, and T is the temperature. Due to the stochastic origins of tfMC and its reliance on a force-bias probabilistic description of the atomic motions, unlike MD, a well-defined (or constant) time step at each iteration of tfMC along the simulation cannot be established. However, in some cases where the variety of complex phenomena expected to be involved in the process being simulated is very limited, one may use the notion of an average time step through the simulation. A statistically relevant average time step in a tfMC simulation could, however, be related to the atomic mean displacement and velocity at a given temperature and is given by

$$\langle \Delta t \rangle = \frac{\Delta}{3}\sqrt{\frac{\pi m}{2k_BT}}, \tag{3}$$

in which m is the mass of an atom. As indicated in [29], depending on the specifics of the simulation system, the tfMC simulation methodology can provide speed-up relative to MD at least by a factor of about 2. More information and in-depth explanation of the tfMC methodology can be found in references [24,26,28,29].

During the tfMC simulations, all atoms in the selected group were displaced using the stochastic tfMC algorithm which is designed to sample the canonical (NVT) ensemble at the desired temperature. The critical parameter that controls (and extends) the effective timescale of the simulation is Δ, which is the maximal displacement length of the lightest atom in the system. In general, the choice of 5%–10% of a typical nearest neighbor distance for Δ can lead to physically meaningful results [26]. Following this criterion, Δ_{Cu} was chosen to be 0.2 Å, and Δ_{TiN} was set to 0.1 Å. Use of these values for Δ_{Cu} and Δ_{TiN} in our sequential MD/tfMC simulations of perfect Cu and TiN crystal structures at 600 K showed that the simulated systems retained their crystallinity and there was no formation of defects; all atoms maintained their original lattice positions and coordination.

When calculating the bulk properties of TiN substrate at 0 K, the system was allowed to change its volume to facilitate relaxation towards zero stresses. A stopping criterion of stress components below 0.1 MPa on all faces of the simulation box was used [44].

The melting point of Cu, described by the MEAM potential used in this study, was estimated by performing several short crystal-liquid coexistence MD simulations with constant temperature and stress normal to the liquid-crystal interface to obtain an initial guess within a

few degrees of the actual melting point followed by one long (10 ns) coexistence simulation with constant enthalpy and stress normal to the crystal-liquid interface [45]. In these simulations, the initial system had 8 × 8 × 96 unit cells (24,576 atoms). More details on the methodology used to estimate the melting point of Cu can be found in the Supplementary Material of [46]. The melting point estimate was $T_m = 1{,}517.8 \pm 0.8$ K in a simulation system in which the crystal-melt interface was parallel to Cu(001) planes. The 600 K value for the temperature used in the Cu/TiN simulations is about $0.395T_m$ and corresponds to about 536 K or 263 °C for real Cu whose melting point is about 1,357 K.

All simulation snapshots were energy minimized to remove thermal vibrations prior to their use for illustration purposes or to conduct various post-processing analyses in OVITO [47]. These analyses include visualization of the simulated atomic structures and displacements as well as detailed crystal structures and defects analysis via the interval common neighbor analysis (ICNA) methodology [48].

2.3. Simulation of deposition and thin film growth using alternating MD/tfMC

As illustrated by Fig. 1, a TiN single crystal substrate having a lattice constant corresponding to the value at 600 K was embedded in a simulation box such that the top of the substrate presented a free surface whose normal direction was parallel to the z axis of the coordinate system. Periodic boundary conditions were imposed in the x and y directions. As explained below, to facilitate a proper substrate thermostatting and to minimize the substrate finite size effect on the physical processes governing the deposition process, the substrate was divided up into four stacked regions labeled: NVE, NVT, NVE, and NVE-boundary with springs (see Fig. 1). The region, labeled NVE-boundary with springs, located at the bottom of the substrate, having a thickness of 5 Å which is equal to the cutoff radius of the MEAM potential, contains TiN atoms which are tethered with harmonic springs to their locations in a perfect crystal. The spring constants were 10 eV/Å, and the spring were applied independently in all three Cartesian directions to mimic their positions and movement within a large bulk region that is thermally equilibrated at 600 K. This type of boundary condition was found to be effective in preventing the simulation system from drifting due to the transfer of momentum from the impinging deposition atoms onto the substrate surface. It should be noted that when compared to the alternative, of completely freezing atom positions, the tethering of the atoms with springs allows them to vibrate and thus facilitates faster temperature equilibration.

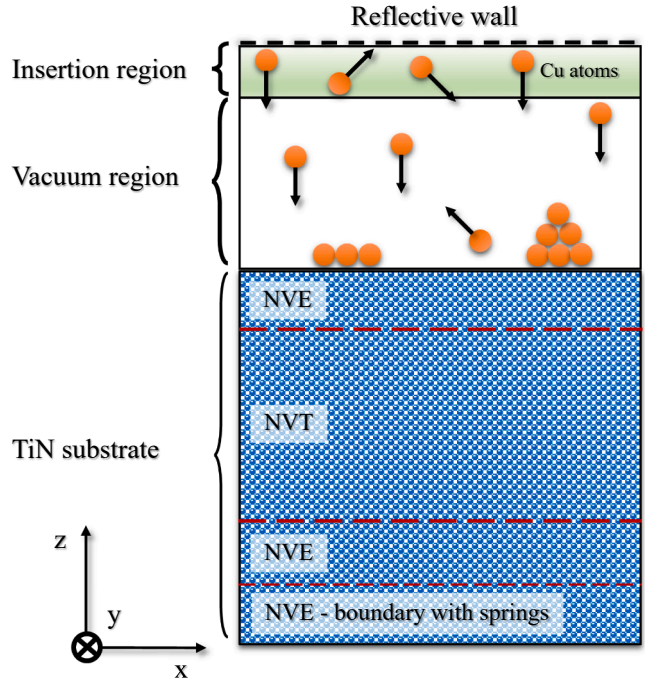

Fig. 1. Schematic representation of the simulation setup for deposition of Cu on a TiN substrate. The deposition of Cu atoms occurs on the free surface of a TiN single crystal slab. Periodic boundary conditions are imposed along x and y axes. The substrate is divided up into four stacked regions labeled: NVE, NVT, NVE, and NVE-boundary with springs. The thermostatting of the system is applied to the NVT region. The depositing Cu atoms are inserted randomly in the insertion region and assigned velocity component only along z direction, as illustrated by black arrows. The dashed line located at the top edge normal to the z direction indicates the location of a reflective wall.

In the MD stage of the sequential MD/tfMC simulation of deposition, most of the kinetic energy of the atoms landing onto the substrate free surface will be converted into heat through successive collisions [25]. To facilitate the heat dissipation, which otherwise would remain trapped inside the system due to imposition of periodic boundary conditions [25], the substrate region labeled NVT in Fig. 1 is thermostatted at the prescribed simulation temperature, and it is "sandwiched" between two buffer regions, labeled NVE in Fig. 1, of the same thickness equal to the cutoff radius of the MEAM potential (i.e., 5 Å). The role of these two buffer regions is to reduce the perturbations induced by the thermostatted region on the trajectories of the other TiN atoms, especially the ones in contact with impinging Cu atoms during their deposition on the surface TiN substrate, and smooth the coupling between the NVT thermostatted region and the NVE-boundary with springs region.

Before the start of the deposition process, the substrate is thermally equilibrated. The thermal equilibration stage is assumed to be complete when the time-averaged temperatures in the two NVE regions reach the prescribed value of 600 K over a sequence of 10,000 MD steps with a standard deviation equal to or less than 2 K. After the equilibration stage, the deposition starts by inserting randomly a specified number of Cu atoms into the insertion region, as illustrated in Fig. 1. The thickness of the insertion region is equal to about two times the cutoff radius of the MEAM potential (i.e., 10 Å), and each newly inserted Cu atom must be located at least a cutoff radius distance from the already existing atoms in both the insertion and vacuum region. The inserted Cu atoms are all assigned the same initial velocity, equal to −1 Å/ps along the negative z direction, as illustrated by black arrows in Fig. 1. During each deposition cycle, about 100 atoms are added to the system. In case of failed adsorption, the Cu atoms are redirected back towards the substrate by their interaction with a reflective wall having a temperature of 600 K, located at the very top of the simulation box and oriented perpendicular to the z direction. The interaction with the reflective wall is Maxwellian, and each reflection is 80% diffusive and 20% specular. These 100 Cu atoms, when arranged into a single FCC(111) layer after depositing onto the TiN substrate of area 6.021 × 5.736 nm^2, yield a substrate surface coverage of about 13.8%, or a film of about 0.14 monolayers (ML). We define the one monolayer (1 ML) of atoms deposited on the substrate as the number of Cu atoms that, when deposited on the surface of the simulated TiN substrate and distributed in a single atomic layer of the same crystallographic arrangement as the deposited single crystal film, yields a full coverage of the substrate. When the amount of Cu deposited exceeds 1 ML, one can also obtain the film average thickness as the product of the number of MLs and the atomic interplanar separation along the growth direction. After 200,000 MD steps, which is long enough to allow the vast majority of Cu atoms to land and be incorporated into the growing film, the atoms still located in the vapor phase are removed from the simulation. It should be emphasized that during the MD deposition stage, we use the Langevin thermostatting in the NVT region due to its efficiency in controlling the fluctuations in temperature caused by the transfer of kinetic energy from the impinging Cu atoms onto the surface, resulting from successive collision events. The end of the MD deposition stage is followed by another thermalization stage in which in the NVT region the Langevin thermostatting is replaced by the Nose-

Hoover thermostatting process that allows for the thermal equilibrium in the NVE regions and the entire system.

After each MD thermal equilibration stage, the system is allowed to further relax by employing a tfMC simulation stage that is performed at 600 K through 500,000 MC steps. It should be noted that the relaxation of the positions of the atoms located in the NVE-boundary with springs region are excluded. However, the forces that contribute to the interaction of these atoms with the other atoms in the system are included in tfMC calculations. After the tfMC simulation stage, to remove the unphysical distribution of atomic potential energies produced by the tfMC algorithm [28] and bring the system back to equilibrium for the next cycle of the deposition handled by an MD simulation stage, a MD thermalization stage in the NVT region, involving the Langevin thermostatting followed by Nose-Hoover thermostatting, is applied as explained previously. In summary, the entire sequential MD/tfMC simulation procedure, as explained above, consists of a cyclic repeat of the following sequence: MD thermal equilibration → MD deposition → MD thermal equilibration → tfMC simulation → MD thermal equilibration…. Thus, the sequential MD/tfMC allows both the fast processes, i.e., capturing atomic impingements on a surface during deposition, and the slower relaxation events (such as thermal relaxation events) associated with the deposition and growth to be represented during the simulation process.

3. Results

3.1. Experimental observations of Cu/TiN orientation relationship and Cu thin film structure

Fig. 2(a) shows data from an XRD symmetric θ/2θ scan of one Cu/TiN/MgO(001) specimen, with a Cu layer growth temperature of 75 °C. With the scattering vector $\vec{K}$ parallel to the growth direction, only MgO(00l) reflections ($l = 2, 3, 4$) are observed, consistent with the substrate being in the [001] orientation. Only TiN(00l) reflections are observed, indicating that the TiN buffer layer is completely textured with TiN(001)//MgO (001) in the growth direction. The only Cu reflection observed is (002), indicating that the Cu layer is also completely textured with Cu(001)// TiN(001)//MgO(001) in the growth direction. Fig. 2(b) shows data from an XRD asymmetric ϕ scan of MgO(024), TiN(024), and Cu(024) reflections obtained from the same Cu/TiN/MgO(001) specimen. Four MgO

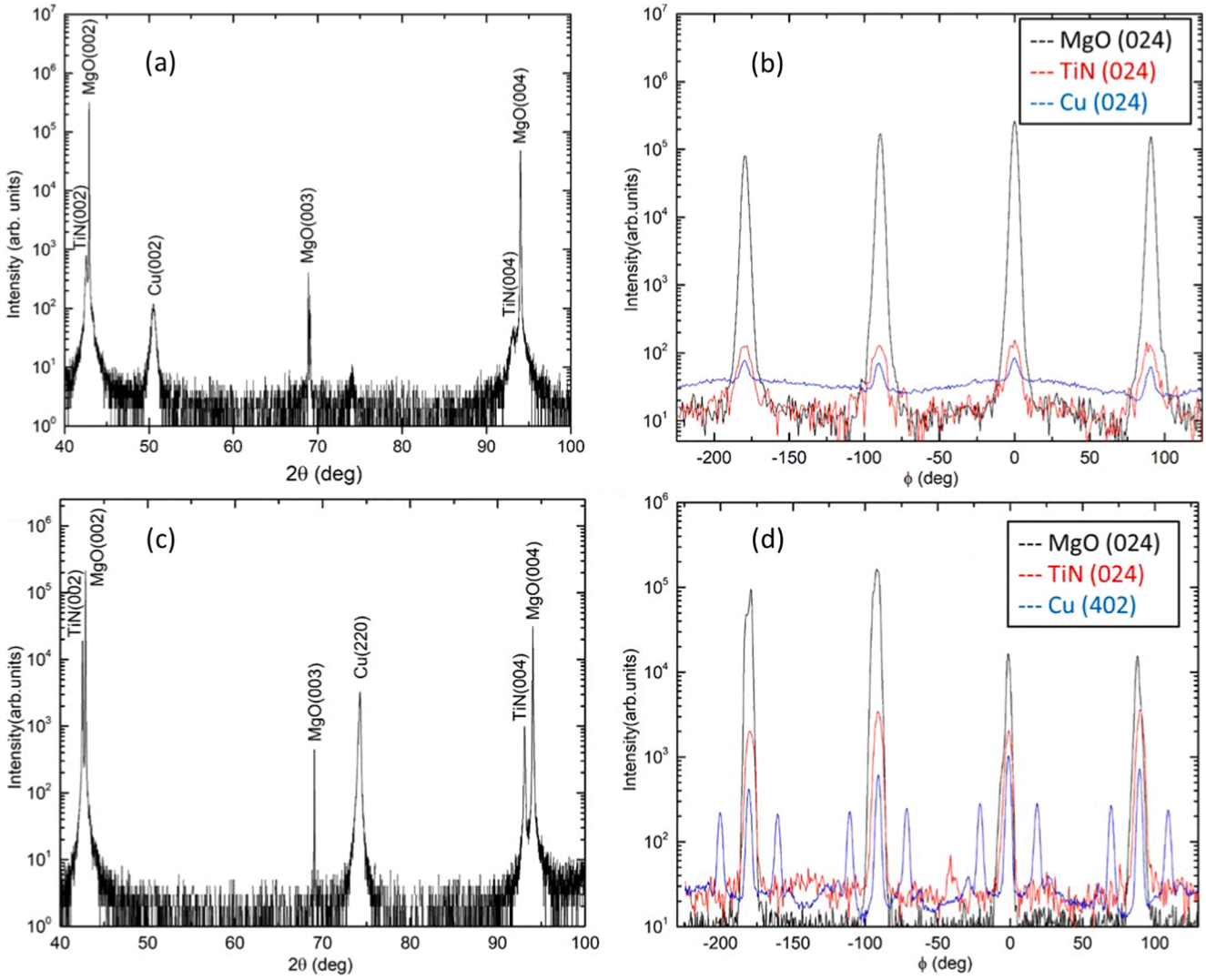

Fig. 2. XRD characterization of Cu thin films grown on TiN(001) templates: θ/2θ scan **(a)** and 360° asymmetric ϕ scan of MgO(024), TiN(024), and Cu(024) reflections **(b)** from one Cu film grown at 75 °C; θ/2θ scan **(c)** and 360° asymmetric ϕ scan of MgO(024), TiN(024), and Cu(402) reflections **(d)** from one Cu film grown at 105 °C.

(024) reflections are observed at 90° intervals, consistent with the single crystal nature of the MgO(001) substrate. Four TiN(024) reflections and four Cu(024) reflections are observed, both completely aligned with the MgO(024) reflections in the ϕ angle. Data in Fig. 2(a) and (b) indicate that both the TiN buffer layer and the Cu top layer are grown on the MgO(001) substrate in the cube-on-cube OR, with Cu(001)//TiN(001)//MgO(001) in the growth direction, Cu[100]//TiN[100]//MgO[100] and Cu[010]//TiN[010]//MgO[010] within the growth plane. In particular, the OR between the Cu top layer and the TiN buffer layer is that of OR_A noted in the introduction.

Fig. 2(c) shows data from an XRD symmetric θ/2θ scan of another Cu/TiN/MgO(001) specimen, with a Cu layer growth temperature of 105 °C. Again, only MgO(00*l*) reflections and TiN(00*l*) reflections are observed, indicating that the TiN buffer layer is completely textured with TiN(001)//MgO(001) in the growth direction. Contrary to data shown in Fig. 2(a), the only Cu reflection observed is (220), indicating a complete but different Cu texture with [110] parallel to the growth direction. The corresponding XRD asymmetric ϕ scan of MgO(024), TiN(024), and Cu(402) reflections from this specimen is shown in Fig. 2(d). The MgO(024) and TiN(024) reflections are again completely aligned in ϕ angle, indicating that the TiN buffer layer is again grown on MgO(001) substrate epitaxially with the cube-on-cube OR. Contrary to data shown in Fig. 2(b), the Cu(402) reflections observed in the ϕ scan form four triplet-peak-groups, separated from each other by 90° in ϕ angle. The middle Cu(402) reflection is aligned with the MgO(024) and TiN(024) reflections. The left and right Cu(402) reflections are separated from the middle (402) reflection by ~19.6°.

The diffraction information presented in Fig. 2(c) and (d) manifest a different epitaxial OR between the Cu layer and the epitaxial TiN(001) buffer layer. Fig. 3 further elucidates this new OR. First, the TiN[100] and Cu$\left[\bar{1}12\right]$ zone axis reciprocal lattice nets are shown respectively in Fig. 3 (a) and (b), from which it is seen that the alignment of the middle Cu(402) reflection with MgO(024) and TiN(024) reflections is consistent with the OR of Cu[110]//TiN[001] in the growth direction and Cu$\left[\bar{1}12\right]$//TiN[100] within the growth plane. Second, keeping Cu[110]//TiN[001] in the growth direction, the in-plane orientation relationship between the Cu top layer and the TiN buffer layer has four symmetry-equivalent variants, Cu$\left[\bar{1}12\right]$//TiN[100], Cu$\left[\bar{1}12\right]$//TiN[010], Cu$\left[\bar{1}1\bar{2}\right]$//TiN$\left[\bar{1}00\right]$, and Cu$\left[\bar{1}1\bar{2}\right]$//TiN$\left[0\bar{1}0\right]$, denoted respectively as variant A, B, C, and D in Fig. 3(c-f). These four symmetry equivalent OR variants, collectively, can be summarized as Cu(110)//TiN(001) in the growth direction and Cu⟨111⟩//TiN⟨100⟩ and Cu⟨112⟩//TiN⟨100⟩ within the growth plane, or OR_B as noted in the introduction and shown in a previous publication by the present authors [16].

It is noted that OR variants A and B are rotated 90° in-plane with respect to each other. In addition, variants A and C are twin-related: forming an in-plane ⟨111⟩ twin with Cu⟨111⟩//TiN[010]. Likewise, variants B and D are twin-related: forming an in-plane ⟨111⟩ twin with Cu⟨111⟩ //TiN[100]. Thus, twins formed from variants A and C and those formed from variants B and D would be rotated 90° in-plane. Fig. 4 (a) and (b) show a TEM BF/DF image pair obtained from the Cu top layer of one Cu/TiN/MgO(001) specimen grown at 105 °C. As reported previously [16], the TEM sample was prepared by OmniProbe lift-out of a thin Cu/TiN slice without the MgO substrate by placing the as-grown Cu/TiN/MgO(001) specimen in the cross section orientation, followed by Ga + ion beam thinning from the TiN side until all TiN is removed. The final sample slice consisted only of the Cu top layer, but originated from an uncontrolled location through the Cu layer thickness. As evident from Fig. 4(b), random shaped Cu domains nestled together to form one continuous Cu layer. The DF image indicates that there are no overlapping domains through the thickness of the TEM sample. As sample slices come from random locations through the Cu layer thickness, it suggests that each domain goes through the entire thickness of the Cu layer. Within each domain, numerous nanoscale twin planes are seen to

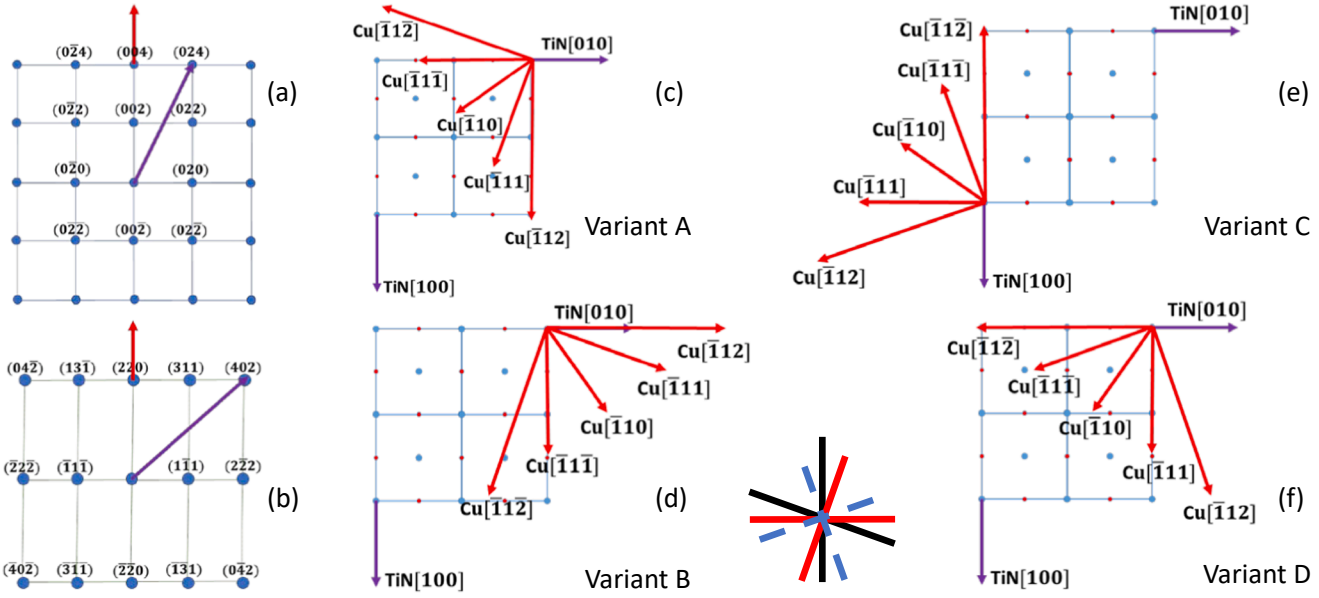

Fig. 3. A schematic of reciprocal lattice nets and real lattice directions for TiN and Cu, with lattice points on the TiN(001) plane as a background: (a) the TiN[100] zone axis reciprocal lattice net; (b) the Cu$\left[\bar{1}12\right]$ zone axis reciprocal lattice net. Red and purple arrows in (a) and (b) denote respectively the film growth direction and the directions of the off-specular XRD ϕ scans shown in Fig. 2; (c) the TiN[100] and [010] lattice directions and various Cu lattice directions within the Cu(110) plane, the in-plane orientation relationship is Cu$\left[\bar{1}12\right]$//TiN[100] and denoted as variant A; (d) a symmetry equivalent OR with Cu[$\bar{1}$12]//TiN[010] and denoted as variant B; (e) another symmetry equivalent OR with Cu$\left[\bar{1}1\bar{2}\right]$//TiN$\left[\bar{1}00\right]$ and denoted as variant C; (f) another symmetry equivalent OR with Cu$\left[\bar{1}1\bar{2}\right]$//TiN$\left[0\bar{1}0\right]$ and denoted as variant D. The inset shows that the in-plane Cu ⟨112⟩ directions from the four variants form a triplet separated from each other by ±19.47° and repeated at 90° intervals (black and red solid lines correspond to variants A and B, blue dashed lines correspond to additional ⟨112⟩ directions arising from variants C and D), consistent with the XRD data shown in Fig. 2.

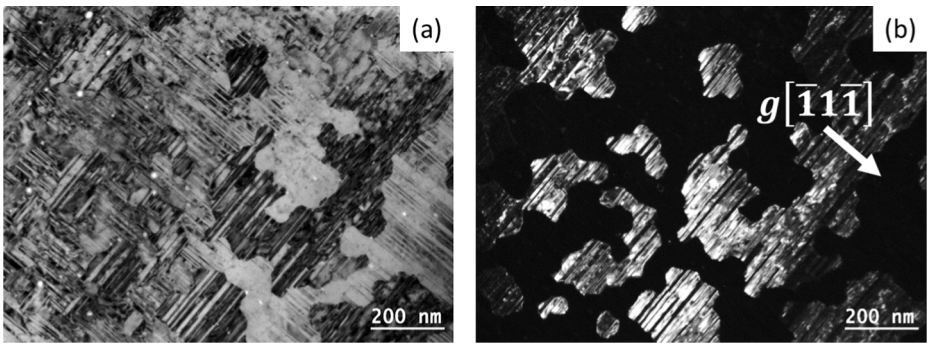

Fig. 4. TEM imaging of the Cu top layer of one Cu/TiN(001) specimen grown on MgO(001) substrate at 105 °C with Cu(110)//TiN(001)//MgO(001): **(a/b)** a BF/DF image pair from the same area of the Cu top layer. The arrow in **(b)** denotes the in-plane direction of Cu$\left[\bar{1}1\bar{1}\right]$. The Cu[110] direction is coming out of the page.

be present perpendicular to the in-plane ⟨111⟩ direction. The typical thickness of the twin platelets is less than 10 nm. The BF image shows that the in-plane ⟨111⟩ nanotwins exist in two mutually perpendicular directions, consistent with the diffraction information presented in Fig. 2 and further elucidated in Fig. 3. The information presented in Figs. 2, 3, and 4 establish unequivocally that Cu thin films can be grown epitaxially on TiN(001) thin film templates in two orientations, OR_A and OR_B. Although the cube-on-cube OR_A between Cu and TiN has been

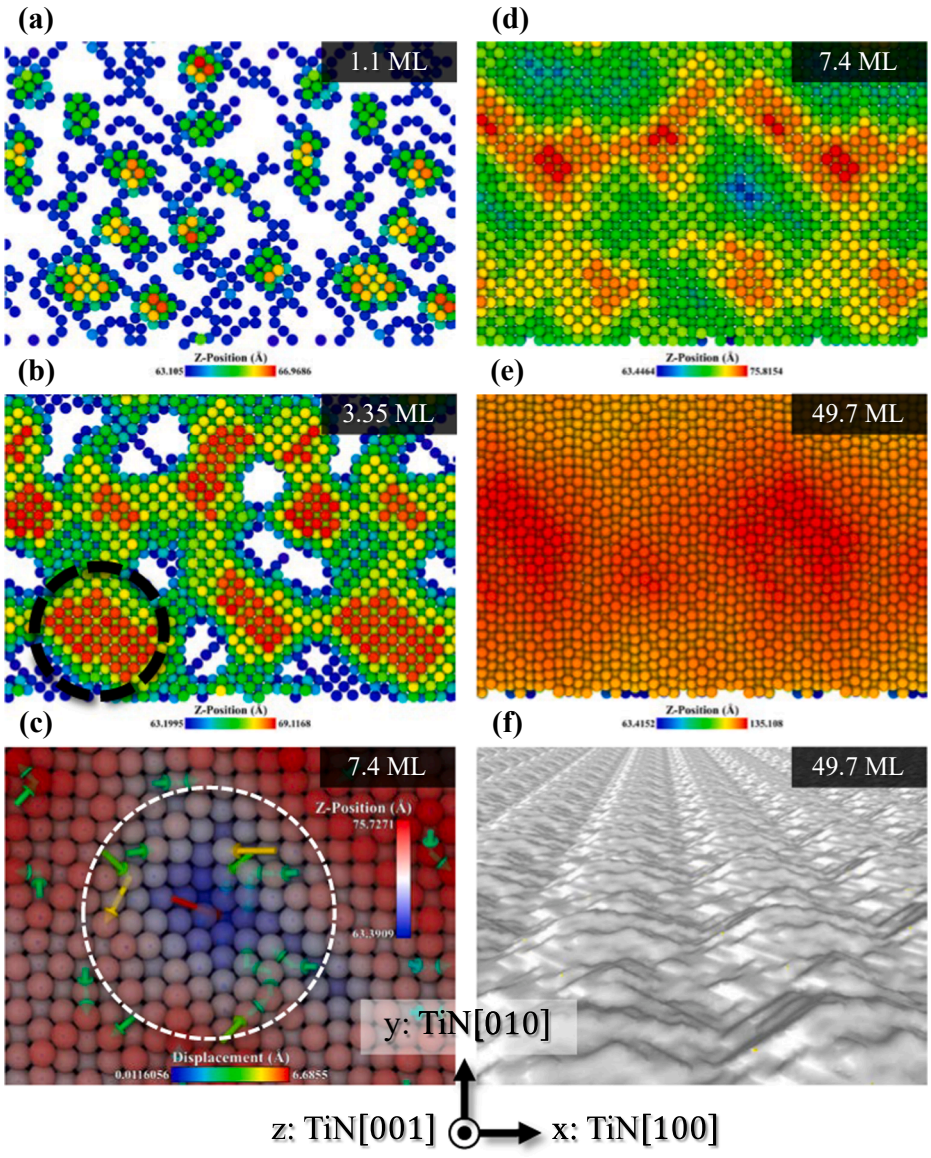

Fig. 5. Snapshots depicting different stages of Cu deposition and growth on TiN(001). The snapshots show the simulated area and its periodic repeat along the x and y directions for better illustration of details. In **(a)-(e)**, Cu atoms are colored according to their position along the z axis, the growth direction. **(a)** Initial 3D growth regime. **(b)** Island coalescence stage. The black dashed circle region indicates a 2D island formed after coalescence. **(c)** Illustration of diffusion of Cu atoms on film surface. The arrows represent the net displacement vectors colored according to their magnitudes. **(d)** Later stage of film growth. **(e)** Overall, nearly 2D thin film growth. **(f)** Silver colored surface mesh showing the morphology of the Cu free surface at the end of the deposition simulation.

reported numerous times in the literature, to the best of our knowledge, OR_B between Cu and TiN was reported for the first time by the present authors in Ref. [16].

While the structural characterization data presented in Figs. 2–4 are clear and unequivocal, the physical mechanisms underlying the experimental observations remain to be elucidated. First, it is puzzling that a slight growth temperature elevation would lead to a completely different orientation relationship between the Cu top layer and the TiN (001) buffer layer. Second, as shown in Fig. 4, dense nanotwins form within the Cu layer with the normal to the {111} twin planes perpendicular to the growth direction. This also differs from other observations made in vapor phase deposited Cu films, where the twin plane normal is reported to be usually parallel to the growth direction [49]. The rest of the paper consists of simulations aimed at providing a deeper physical understanding of the mechanisms responsible for the experimental observations described above.

3.2. MD/tfMC simulations of Cu deposition on TiN(001) substrate

First, to determine which stoichiometric surface orientations of TiN are energetically more favorable or stable, various crystallographic orientations were examined, the results of which can be seen in the Supplementary Information file. It was found that the Ti-terminated TiN (111) has the lowest surface energy (SE), followed by TiN(001). Among various orientations for TiN, TiN(111) and (001) surfaces have been the most commonly reported ones in the literature [15,16,50–58]. Our focus will therefore be on the flat surfaces of TiN(001), N-terminated TiN (111), and Ti-terminated TiN(111).

Up to 22,024 Cu atoms were deposited on a TiN(001) substrate consisting of a 27,000 atoms TiN slab of dimensions 6.386 × 6.386 × 6.362 nm^3 with edges aligned along x//TiN[100], y//TiN[010], and z//TiN[001], respectively. The 22,024 Cu atoms, when distributed onto FCC(1 1 0) atomic planes stacked on the TiN substrate of area 6.386 × 6.386 nm^2, leads to the formation of a 49.7 ML (~63.41 Å) thick film. In agreement with experimental observations [57,59–62], the analysis of the snapshots of different stages of Cu deposition and growth simulation, provided in Fig. 5(a) through (e) and Movie 1(a), shows the initial island growth, island coalescence, and overall film growth of Cu on TiN(001). At the early stage of deposition, due to stronger Cu-Cu interaction compared to that for Cu-TiN(001), Fig. 5(a) shows that 3D Cu islands start to grow randomly on the substrate. Then, as indicated by dashed black circle in Fig. 5(b), these islands coalesce and gradually wet the entire substrate while the film thickness increases by the growth of 2D islands. As can be observed from Fig. 5(c), due to a sufficiently low Ehlrich-Schwöbel (ES) barrier, Cu surface atoms located closer to the tops of the islands, colored by red within the region bounded by the white dashed circle, descend and occupy the valley-like spaces changing the film morphology to one with nearly uniform thickness. This downhill diffusion of Cu atoms is shown in Fig. 5(c) in which the net displacement vectors between the initial (before the relaxation) and

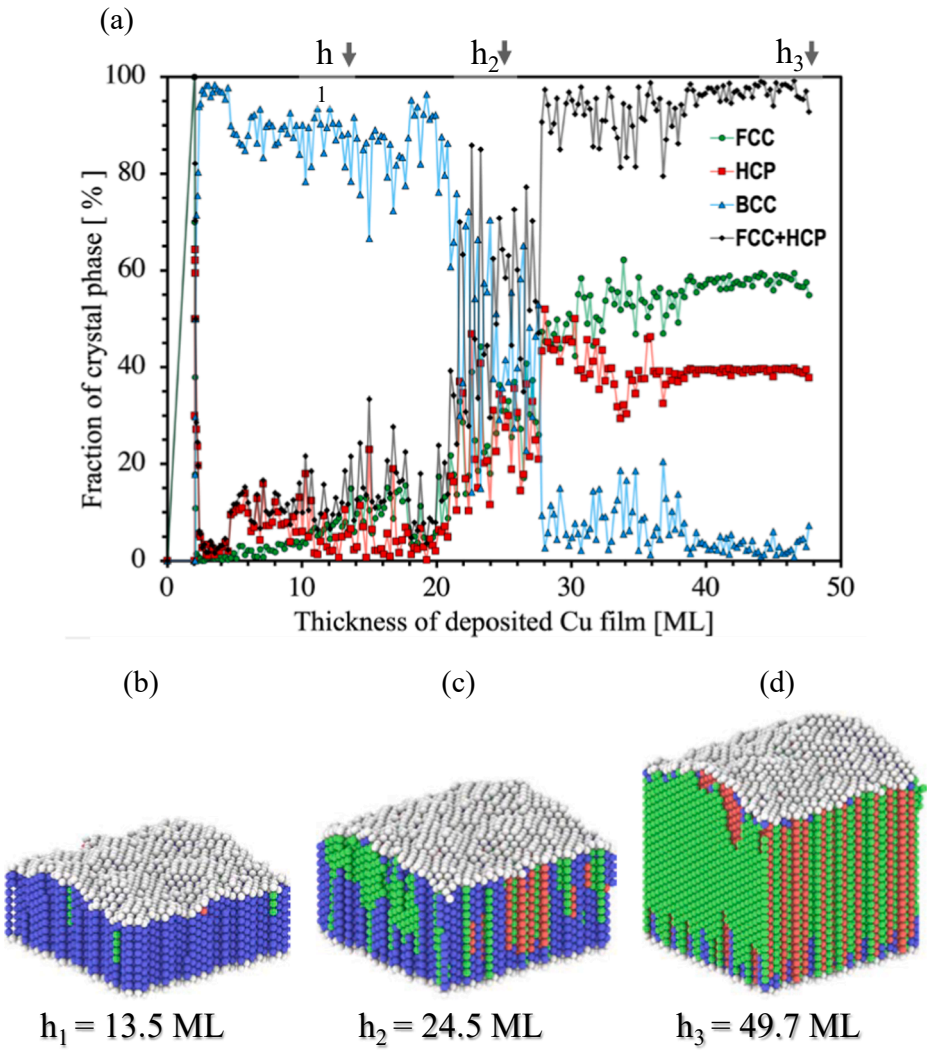

Fig. 6. (a) Variation of the fractions of BCC, FCC, and HCP crystal phases (crystal structures) present in the deposited Cu film as a function of the Cu film thickness (expressed in equivalent number of Cu(110) monolayers (ML)). The atoms belonging to a specific phase were identified by ICNA of the corresponding relaxed and quenched simulation structures. The snapshots in **(b)**, **(c)**, and **(d)** show the film structures and crystalline phases present after deposition of approximately 13.5, 24.5 and 49.7 ML. The three film thicknesses are also indicated in (a). The atoms located in the different phases were identified by ICNA and colored according to the following rule: blue are BCC, red are HCP, green are FCC, and light-gray are atoms with no assigned crystal structure.

final positions (after the relaxation) of the atoms are illustrated, and the arrows were colored according to their magnitudes. In the region marked by the white dashed circle in Fig. 5(c), the atomic displacements indicate that the Cu atoms diffuse directly or via a chain of diffusion events from surface regions with higher elevation, depicted by red-colored atoms, toward the substrate and valley-like spaces, illustrated by dark blue colored atoms. In addition, Movie 1(b) illustrates the net atomic displacements of Cu atoms, colored based on their magnitudes, after the relaxation. Moreover, Fig. 5(f) depicts the Cu film free surface at the end of the deposition simulation. The surface morphology of the simulated film resembles the lenticular morphology observed in our previous experiments of Cu deposition on TiN(001) at 105 °C [16].

By first minimizing and then using the relaxed and thermally equilibrated configurations of the Cu/TiN system, after each MD/tfMC deposition sequence, ICNA was conducted to analyze the various defects and crystal phases (crystal structures) present in the growing Cu film during the deposition process. No misfit dislocations network (MDN) structure was identified between Cu and TiN, and it was determined that Cu grows pseudomorphically on TiN. Fig. 6(a) depicts the presence of different crystal phases and the change of their fraction during the deposition process. Three crystal phases of BCC, FCC, and HCP were identified in the Cu film, and the evolution of their fraction is plotted as function of the film thickness (expressed in the number of Cu {110} MLs). According to the trends seen in Fig. 6(a), during the early stage of growth, the BCC phase dominates the film structure, and its fraction decreases slightly as the FCC and HCP phase fractions increase slightly until the film thickness reaches about 13.5 ML. Beyond this film thickness, the BCC phase fraction starts to decrease rapidly while the fraction of the FCC+HCP phases experience a concomitant rapid increase. These BCC and FCC+HCP fractions are equal when the film thickness is about 24.5 ML, beyond which the BCC and FCC+HCP phase fractions continue to monotonically decrease and increase, respectively, albeit at much lower rates. As the deposition process continues, the fraction of the FCC+HCP phases approaches a plateau at about 97% when the film thickness is approximately 49.7 ML (~63.41 Å). Important structural characteristics of the growing Cu film are illustrated in Fig. 6(b), (c), (d), and Movie 2, in which the atoms are colored according to their local crystal structure ordering. This series of snapshots shows how the BCC-Cu phase transforms to the FCC+HCP phase in which the following orientation relationships can be determined:

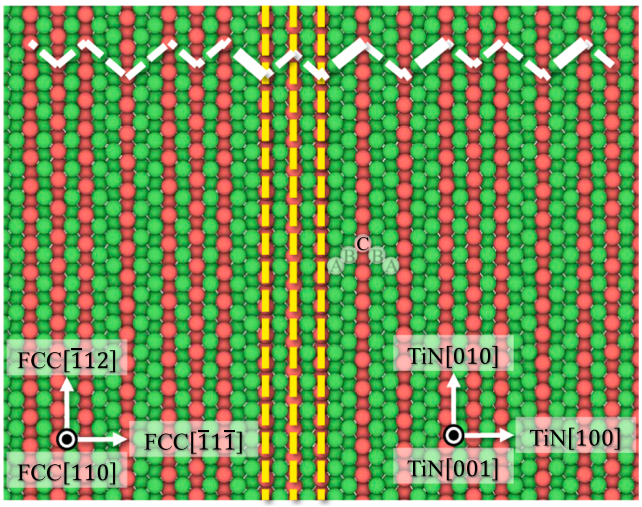

Fig. 7. Atomic arrangement shown in a cross section plane taken from the middle of the Cu thin film grown on the TiN(001) substrate, depicted in Fig. 6 (d). The structural analysis reveals that the thin film contains numerous Cu nanotwins with twin boundaeries oriented parallel to the film growth direction. The twin boundary atoms having HCP coordination are colored in red, and those in FCC coordination are colored in green. Some twin boundaries have been marked by yellow dashed lines and a stacking sequence of …ABCBA… to identify them more easily. The white dashed lines show the conjugate twinning planes. The snapshot shows its periodic repeat along the x and y directions for better illustration of details.

3.3. MD/tfMC simulations of Cu deposition on N-terminated TiN(111) substrate

We deposited 7,006 Cu atoms on the N-terminated TiN(111) surface of a TiN slab of dimensions of 5.736 × 6.021 × 6.610 nm^3 with edges aligned along x//TiN$\left[\bar{1}\bar{1}2\right]$, y//TiN$\left[1\bar{1}0\right]$, and z//TiN[111], respectively, containing 21,105 atoms. The 7,006 Cu atoms, when distributed onto FCC(111) atomic planes stacked on the TiN substrate of area 5.736 × 6.021 nm^2, leads to the formation of a 11.12 ML (~23.17 Å) thick film. As illustrated by Fig. 8(a) and Movie 3(a), during the early stage of growth, 3D islands nucleate randomly on the N-terminated TiN(111) substrate. Since the interaction between Cu and N atoms is relatively weak, the wettability of Cu on the substrate is poor. Therefore, the deposited Cu atoms diffuse rapidly on the substrate and facilitate the nucleation of 3D islands or attach and incorporate into existing ones. This mechanism has been illustrated in Fig. 8(a) and (b) in which the regions delimited by the solid white circles depict the growth of a larger island during deposition. Further growth of 3D Cu islands is also promoted by the coalescence of neighboring islands, as illustrated in Fig. 8 (b) and (c) in the regions delineated by the solid white rectangular frame, in which the white arrows indicate the direction of movements of the neighboring islands toward the center of mass during coalescence.

Movie 3(b) and Fig. 9 illustrate the net displacement vectors of atoms during neighboring islands coalescence events after minimizing the configuration corresponding to the tfMC relaxation and subsequent MD thermal equilibration. As the size of the islands increases due to continued deposition, Fig. 8(c) through (g) together with related net

$$\text{BCC-Cu}[110]//\text{TiN}[100] \rightarrow \text{FCC-Cu}\left[\bar{1}\,1\bar{1}\right]//\text{TiN}[100] \qquad \text{BCC-Cu}\left[\bar{1}10\right]//\text{TiN}[010] \rightarrow \text{FCC-Cu}\left[\bar{1}12\right]//\text{TiN}[010] \qquad \text{BCC-Cu}[001]//\text{TiN}[001] \rightarrow \text{FCC-Cu}[110]//\text{TiN}[001]$$

According to (4), crystal orientation in the growth direction of BCC-Cu[001]//TiN[001] changes to FCC-Cu[110]//TiN[001], which is the same as the growth direction related to OR_B revealed in the experimental results shown in Section 3.1.

Additional insights into the microstructure development was obtained by performing serial sectioning and analysis of the growing Cu film. Fig. 7 depicts the atomic arrangement in one plane in the 49.7ML (~63.41 Å) thick Cu film illustrated in Fig. 6(d), with normal along the growth direction, i.e., FCC-Cu[110]//TiN[001] or normal to TiN(001) surface. Fig. 6(d) and 7 reveal that nanotwinned FCC-Cu with HCP twin boundaries develop throughout the entire thickness of the film. The characteristics of the nanotwinned FCC-Cu structure, shown in Fig. 7, are in excellent agreement with those observed in the micrograph shown in Fig. 4, where the normal of the nanotwin planes is perpendicular to the growth direction. The twinned structure in Fig. 7 resembles that corresponding to variant B shown in Fig. 3(b).

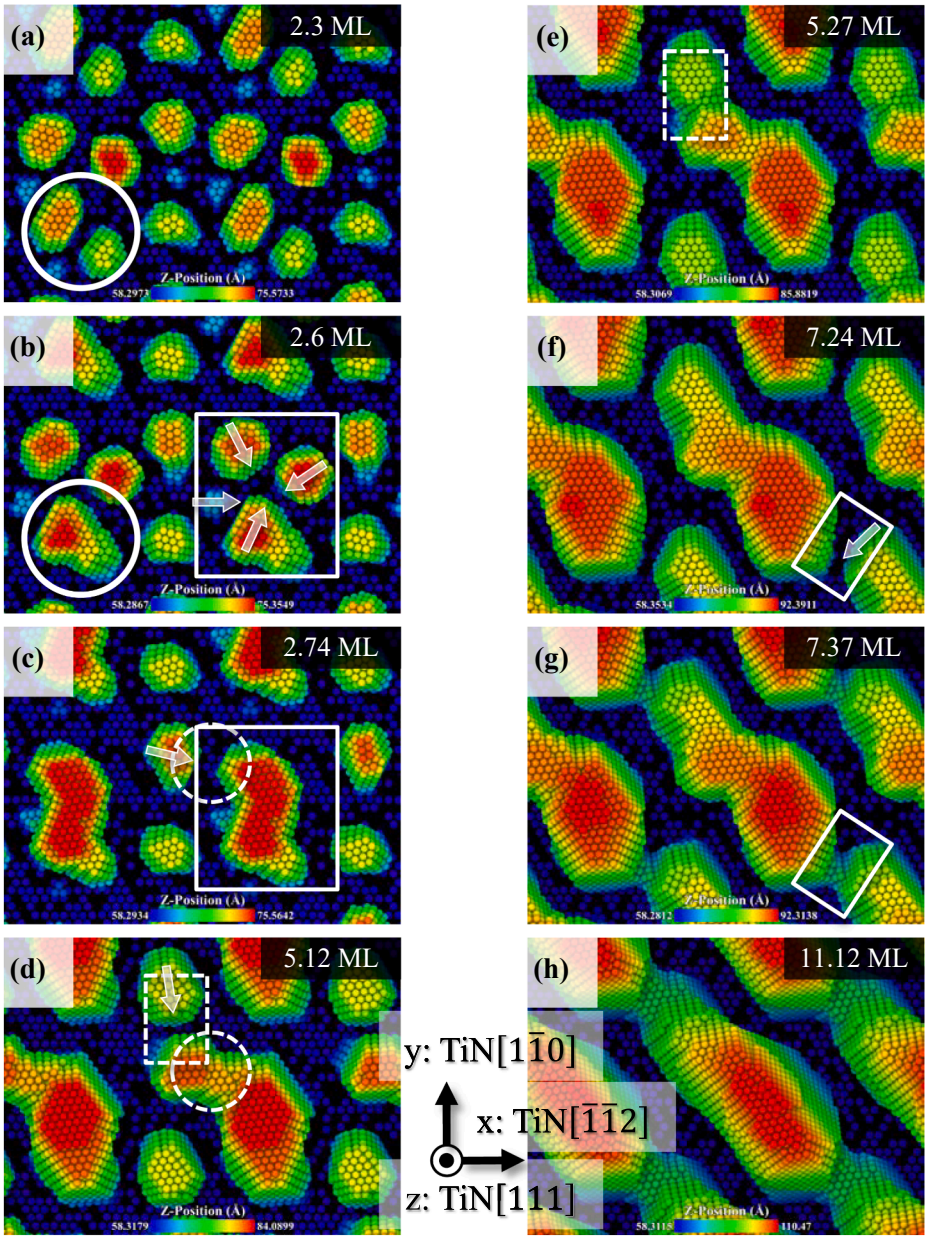

Fig. 8. **(a)** to **(h)** sequence of snapshots for different stages of Cu deposition and growth simulation on N-terminated TiN(111). For clarity of illustration, the TiN substrate is not shown. Cu atoms are colored according to their position along the z axis. White objects are used to trace the movements of the islands more easily, and the white arrows represent the movement of the islands during the relaxation. Snapshots have been repeated along the periodic directions of x and y for better illustration of details.

atomic displacement vectors shown in Fig. 9(b) to (d) demonstrate that often the coalescence happens through bridge formation between neighboring islands. Through this process, the smaller islands are attached to or absorbed into the larger ones.

It is worth mentioning that, as seen in Movie 3(b) and Fig. 9, our simulations reveal that during island coalescence, the atoms located on the islands facets are displaced by notable amounts; up to ~1 or 2 nm in some cases. This mass transport mechanism on facets of islands is in agreement with the results of kinetic Monte Carlo simulation studies in which it was reported that the coalescence of 3D islands on a weakly-interacting substrate is accompanied by repeated facet migration [32].

As depicted in Fig. 8(h), during further island growth, because of shadowing instability [63], the large and tall Cu islands intercept the flux of incoming Cu atoms more often, resulting in their faster growth. This growth mechanism is in agreement with the experimental observation in [62] where during the early stages of Cu deposition on a TiN substrate pretreated with N_2 plasma, the wetting angle between the Cu islands and the substrate based on Young's equation was found to be 90°. One may infer from these observations that Cu deposition on weakly interacting N-rich TiN substrates may not produce continuous thin films, and it is likely for the deposited material to develop notable porosity during growth [63].

In addition, Fig. 10 depicts the top view of the growing film where one can observe how a large Cu island becomes larger and taller due to the nucleation and growth of 2D islands on its facets. As it can be seen from Fig. 10(a), the surface of the island is mostly composed of {100} and {111} flat facets. The top {111} facet of the island intercepts the incoming Cu species, and subsequently, a 2D island starts to grow due to diffusion of the deposited Cu atoms to kink sites. Afterward, 2D islands grow from the ridges of the top {111} facet along the {111} and {100} side walls, and the islands grow in different directions on the facets, as shown in Fig. 10(b) through (f). At the very early stage of growth as in Fig. 8(a), the structural analysis shows the presence of BCC phase in some of the small islands, but that phase fades away quickly after coalescence of islands. Therefore, the FCC and HCP Cu phases dominate in the deposited Cu atoms, and the islands grow along the direction of FCC-Cu(111)//TiN(111).

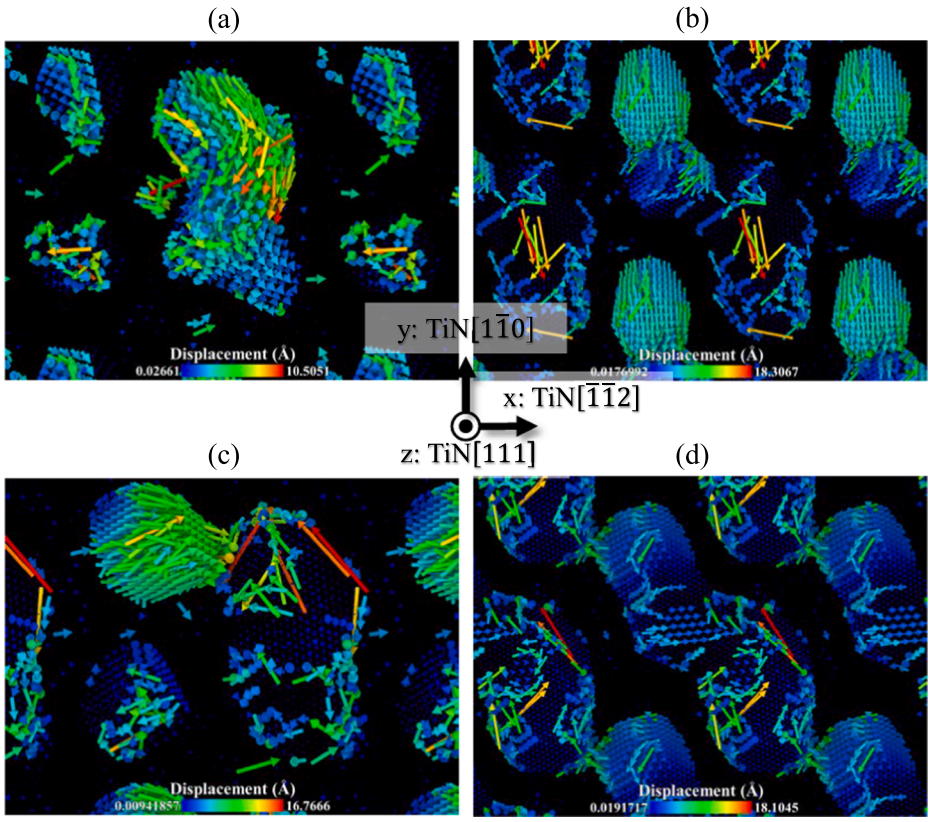

Fig. 9. Depiction of net atomic displacements associated with different stages of islands coalescence events depicted in Fig. 8: **(a)** Fig. 8(b-c), **(b)** Fig. 8(c-d), **(c)** Fig. 8 (d-e), and **(d)** Fig. 8(f-g). The arrows represent the net displacement vectors colored according to their magnitudes.

3.4. MD/tfMC simulations of Cu deposition on Ti-terminated TiN(111) substrate

A Ti-terminated TiN(111) substrate with 22,880 TiN atoms and dimensions of 5.736 × 6.021 × 6.450 nm^3 along x//TiN$\left[\bar{1}\bar{1}2\right]$, y//TiN$\left[1\bar{1}0\right]$, and z//TiN[111], respectively, was used to grow Cu films containing up to 10,299 atoms. The 10,229 Cu atoms, when distributed onto FCC{111} atomic planes stacked on the TiN substrate of area 6.021 × 5.736 nm^2, yield a film about 16.35 ML (~34.07 Å) thick. In contrast to the N-terminated TiN(111) substrate, Cu deposited on the Ti-terminated TiN(111) shows high degree of wettability such that the Cu atoms completely wet the TiN surface first, and then, the Cu layers initially grow via nucleation and growth of 2D islands, as presented by Fig. 11(a) and Movie 4(a). However, during further growth, as illustrated by Movie 4(c) and Fig. 11(b) through (d), overcoming the ES barriers to cross over the steps becomes difficult for the Cu adatoms, and Schwoebel instability occurs which is manifested by hindered atomic surface diffusion toward the lower surface regions which are surrounded by steps going down [63]. In other words, because of a decrease of adatoms diffusion flux from the upper terraces toward the lower terraces, new layers are nucleated on top of the existing islands, and the growth is biased toward the vertical direction relative to the lateral directions.

Based on ICNA, as shown in Fig. 12(a) and Movie 4(c), the deposited Cu film has FCC and HCP crystal structures with the growth direction of FCC-Cu[111]//TiN[111] such that FCC-Cu$\left[\bar{1}\bar{1}2\right]$//TiN$\left[\bar{1}\bar{1}2\right]$ and FCC-Cu$\left[1\bar{1}0\right]$//TiN$\left[1\bar{1}0\right]$. This orientation relationship is in accordance with experimental observations reported in [50,53]. Also, in agreement with experimental observations of ⟨111⟩ direction Cu growth with nanostructured growth twins [49], Fig. 12(a) and Movie 4(c) reveal that a 2-layer thick nanotwin is formed close to Cu(111)//Ti-terminated TiN (111) interface. The stacking sequence of …ABCBA… in Fig. 12(a) depicts where the twin boundary with HCP structure and red colored atoms is located, and it has been marked by a dashed black line.

In addition, to accommodate the misfit strain of 14.3% generated at 600 K according to the orientation relationship between Cu and TiN mentioned previously, a MDN forms at the semi-coherent interface of Cu (111)//Ti-terminated TiN(111) with either triangular or hexagonal structure, both of which are 3-fold symmetric. The MDN can be visualized by coloring Cu atoms based on the structure obtained from ICNA analysis as in Fig. 12(b) and Movie 5(b) or by using potential energy per atom for Cu, Ti, or N as in Fig. 12(c), (d), (e) and Movies 5(a), 5(c), or 5 (d), respectively. As it can be seen from Fig. 12(b), the MDN structure in Cu(111) at the interface of Cu(111)//Ti-terminated TiN(111) is composed of FCC triangular patches with atoms colored in green and intrinsic stacking faults with triangular shapes having HCP structure indicated by red colored atoms. In Fig. 12(c), the misfit dislocations and nodes related to the MDN structure in Cu are marked by yellow lines and transparent yellow circles, respectively. By comparing the potential energy per Cu atom map shown in Fig. 12(c) to the one for Ti atoms in the first layer of TiN close to the interface shown in Fig. 12(d) or N atoms in the second layer of TiN as in Fig. 12(e), one can recognize that the MDNs are composed of nodes with different structures. Also, Movies 4 (b) and 5(b) illustrates that during the relaxation or translation of the MDN, complex shuffling of atoms in the cores of nodes occurs, and often, they are translated as well as the MDN. It should be noted that Cu (111)//Ti-terminated TiN(111) interface is typical of {111} interfaces in FCC materials with low shear strength [64]. Therefore, it can be realized from Movies 4(b) and 5(b) that the entire MDN can translate in a rigid manner in different directions, due to minimal pinning offered by the nodes of the MDN [19] and having an isotropic in-plane plastic response as a result of 3-fold symmetry in the MDN structure [19] shown in Fig. 12(b) through (e).

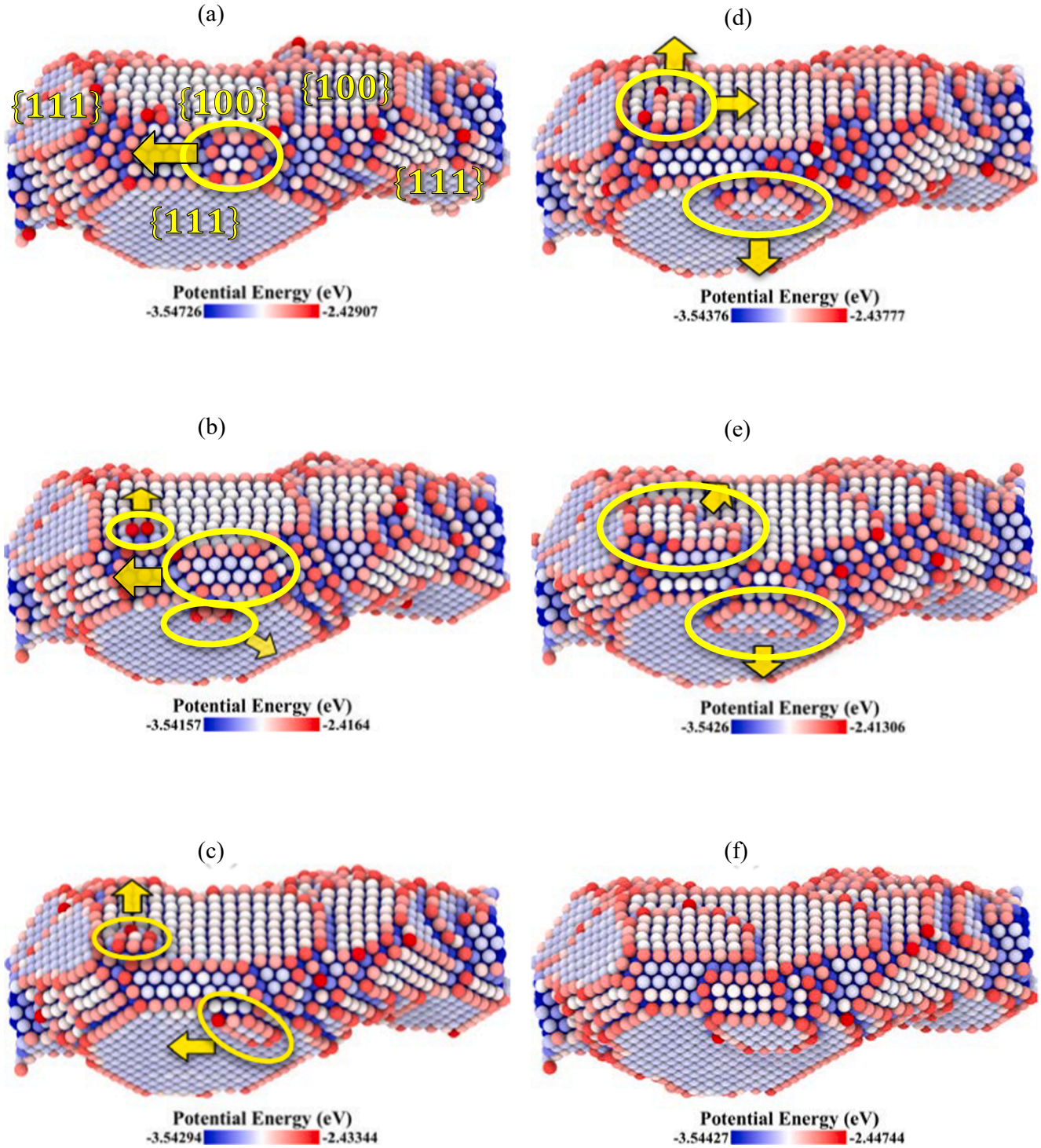

Fig. 10. **(a)** to **(f)** Sequence of snapshots, from the simulation of Cu deposition on a N-terminated TiN(111) substrate, depicting different stages of growth of a Cu island. The TiN substrate is not shown for clarity of illustration. Cu atoms are colored according to their potential energies. The yellow arrows represent the growth direction of 2D islands.

The MDN structure in Fig. 12(b) through (e) is typical in bi-material systems, such as Cu/Ag, where a MDN is formed to accommodate a large lattice mismatch between constituent materials of the system [64]. This type of MDN structure shows notably small interface nodal spacing which is less than ~2.5 nm for "smeared" nodes [64] at the Cu(111)//Ti-terminated TiN(111) interface in Fig. 12(b) through 12(e). Therefore, straight dislocations with edge character are formed to reduce interaction energy among nodes and dislocations while the self-energy of the nodes and dislocations are being minimized [64]. Furthermore, since the MDN accommodates the lattice mismatch, its Burgers vectors are parallel to the interface [19]. As it can be observed from Fig. 12(c), these dislocations are aligned with ⟨110⟩ directions and have $(a_{Cu}/6)\langle 112\rangle$ Burgers vectors of Shockley partials indicated by white arrows in this figure with a_{Cu} being the lattice constant of Cu at 600 K.

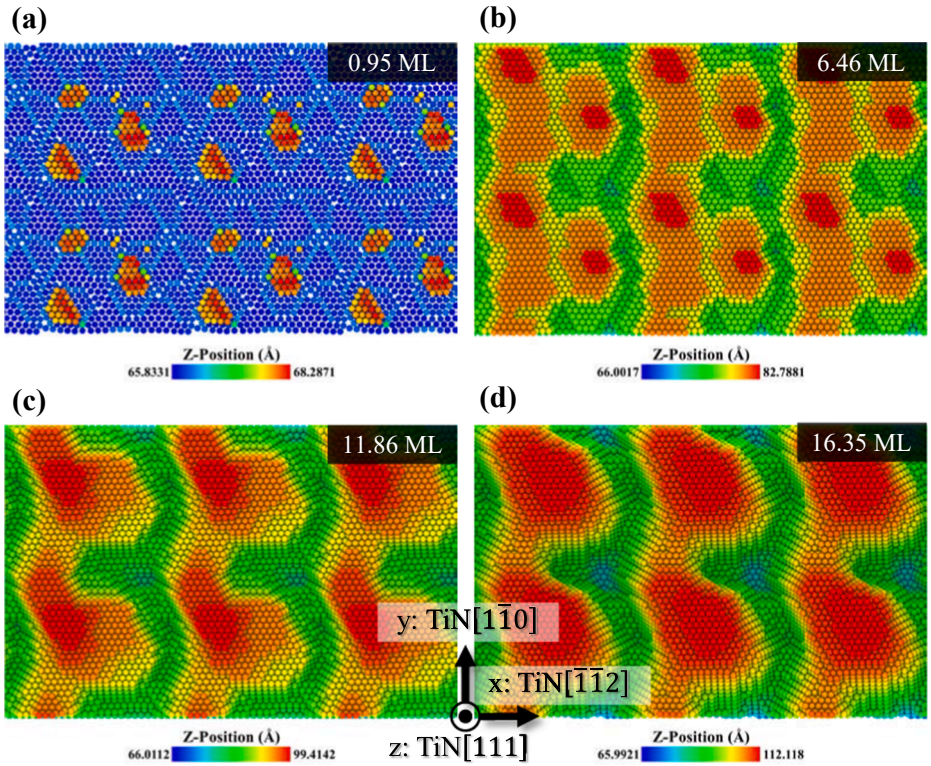

Fig. 11. Sequence of top view snapshots **(a)** through **(d)**, from the simulation of Cu deposition on a Ti-terminated TiN(111) substrate, showing different stages of Cu thin film growth. The TiN substrate is not shown for clarity of illustration. Cu atoms are colored according to their position along the growth direction (z axis). Snapshots have been repeated along the periodic directions of x and y for better illustration of details.

4. Discussion

Typically, for substrate temperatures in the 300 K to 500 K range, Cu (001) grows with a cube-on-cube epitaxial relationship on a TiN(001) substrate [16,65], or OR_A in Fig. 2(a) and (b). However, the growth of epitaxial Cu/TiN in OR_A is thermodynamically unfavorable due to a large lattice mismatch of 14.25% between the film and the substrate [16,65], and a MDN is formed to accommodate the induced in-plane strain due to the lattice mismatch [16,65]. Therefore, the epitaxial Cu/TiN OR_A film growth at low temperatures can be attributed to kinetically-hindered surface diffusion or limited surface kinetics which can become more restricted due to formation of misfit dislocations [65]. As illustrated in Fig. 2(c) and (d) and Figs. 3–7 and Movies 1–2, the OR_B orientation, facilitated by the higher temperature of the TiN(001) substrate, can be linked to the increased diffusivity of Cu atoms on the surface of the growing film mediating the growth of a more favorable configuration of BCC-Cu in the early stage of growth.

In general, the balance of crystalline phases present in a thin film grown on a substrate at equilibrium is determined by the competition among interfacial energy, surface energy, and bulk energy [66]. By tallying the contributions from these three energy terms, one can argue that at the early stage of Cu thin film growth, the film with BCC-Cu(001)//TiN(001) with the orientation relationship in Eq. (4) should have a lower formation energy than that of FCC-Cu(001)//TiN(001). Simple estimates of the energies of the film-substrate system having the two crystal phases and the corresponding orientations can be given as follows. First, by disregarding the strain energy contribution [66], the calculated cohesive energies of the relaxed crystal structures at 600 K are −3.46 eV for FCC-Cu and −3.45 eV for BCC-Cu, values which indicate that the bulk energy of the BCC phase is just only slightly above that of the FCC phase. Second, as documented in the Supplementary Information, the surface energy calculations, based on the MEAM potential used here, give the value of 1409 mJ/m^2 for FCC-Cu{100} free surface while the surface energy is 1401 mJ/m^2 for BCC-Cu{100} free surface. Thus, the surface energy term slightly favors the BCC film. Third and more importantly, it can be argued that at the early stage of Cu thin film growth, the BCC-Cu(001)//TiN(001) system should have a lower interface formation energy than that of FCC-Cu(001)//TiN(001). This can be rationalized by considering the crystal structure and the mechanical properties of the films in terms of the lattice mismatch and elastic constants at 600 K that were calculated and are presented in Table S1 in Supplementary Information. To this end, first, the in-plane strain magnitudes associated with the Cu/TiN lattice mismatch can be introduced in the Cu material only [67], and then, the normal stress component along the direction pointing toward the free surface of the film, i.e., [001] for both FCC-Cu and BCC-Cu, is set to zero to obtain in-plane stresses in the Cu thin film. In the case of FCC-Cu(001)//TiN(001) with the lattice mismatch of 14.25%, the in-plane stress components become ~12.6 GPa on average in each direction. In contrast, in the case of BCC-Cu(001)//TiN(001) with the lattice mismatch of 3.64%, the stress magnitudes were calculated to be ~0.6 GPa. This formation of BCC-Cu represents a substantial reduction in the stress magnitudes and can be the main reason that no MDN is required to be formed to relive high stress magnitudes as in the case of FCC-Cu(001)//TiN(001). Therefore, BCC-Cu(001) grows pseudomorphically on TiN(001) up to ~20 ML thick, as shown in Fig. 6(a) and (b) and Movie 2. In summary, up to ~20 ML in Fig. 6(a), the bulk energy may not play a key role, whereas both interfacial and surface energy differences should drive the Cu/TiN system to reach BCC-Cu(001)//TiN(001) once the substrate temperature is high enough to facilitate sufficient Cu surface diffusion on TiN(001) surface.

However, as revealed by Fig. 6 and Movie 2, the increase of the thickness of deposited Cu thin film on TiN(001) substrate beyond ~20 ML results in transformation of the BCC-Cu to nanotwinned FCC-Cu with twins developed through the entire thickness of the film. As mentioned above, this phase transformation may not be driven only by cohesive

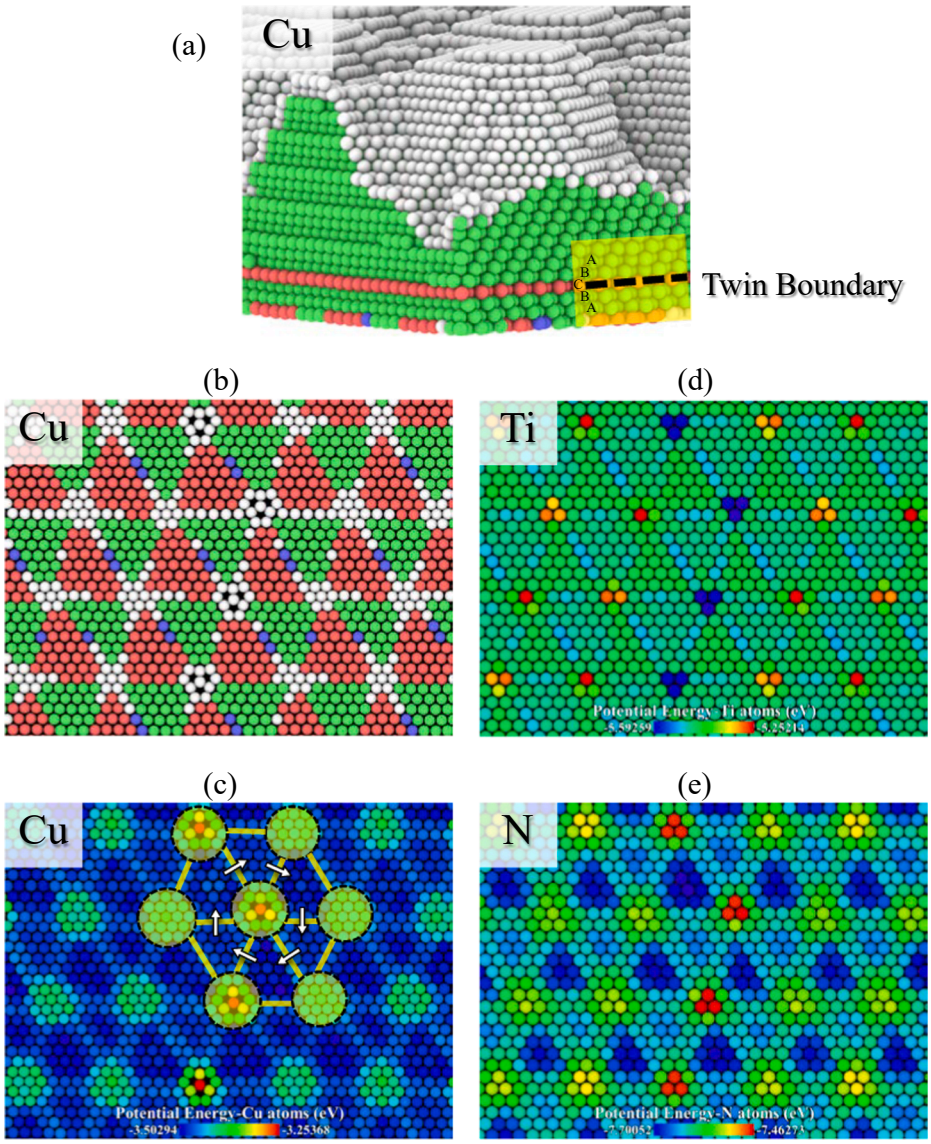

Fig. 12. (a) Deposited Cu atoms are colored by crystal structure using ICNA analysis on Ti-terminated TiN(111). **(b)** Atoms colored by ICNA for the Cu layer at the Cu(111)//Ti-terminated TiN(111) interface. For ICNA, blue means BCC, red relates to HCP, green pertains to FCC, and white is assigned to atoms with unidentified structure. **(c)** Same view as (b), but atoms are colored by potential energy per Cu atom where the MDN nodes and misfit dislocations have been marked via transparent circles and yellow lines, respectively. The white arrows show $(a_{Cu}/6)\langle 112\rangle$ Burgers vectors of Shockley partials associated with yellow straight dislocations with pure edge character aligned with $\langle 110\rangle$ directions, where a_{Cu} is the lattice parameter of Cu at 600 K. **(d)** Closest Ti layer to the interface colored by potential energy per atom. **(e)** Closest N layer to the interface colored by potential energy per atom. Snapshots have been repeated along the periodic directions of x and y, and TiN substrate is not shown for better illustration of details.

energy differences between unstrained FCC-Cu and BCC-Cu, due to the slight difference that exists between them. Therefore, reducing the strain energy component of the bulk energy can be an important factor here, as it increases in linear proportion to the film thickness. Fig. 5(c) and Movie 1(b) demonstrate that diffusion of atoms occurs only on the surface of the Cu thin film, and as it can be seen in Movie 1(b), the cooperative atomic displacements in bulk-like regions of the Cu thin film occurs only below the surface of the Cu, implying that the transformation of the BCC-Cu to the nanotwinned FCC-Cu in Figs. 4 and 7 should be martensitic in nature.

To further examine a potential stress-driven martensitic transformation of BCC-Cu to nanotwinned FCC-Cu, a MD simulation is set up with the following details and assumptions. Noting that BCC-Cu to nanotwinned FCC-Cu phase transformation occurs in a bulk region between the Cu/TiN interface and the Cu free surface, as shown in Fig. 6 and Movie 2, BCC-Cu atoms are arranged according to their perfect crystal lattice positions at 600 K within a fully periodic simulation box. Then, a spherical void with a 2 nm diameter is created in the center of the computational cell to allow for activation of possible defect-assisted deformation mechanisms, thanks to the high concentration and complex distribution of stresses around the void [68]. Afterward, by using a NVT simulation followed by a NPT one, the system is relaxed volumetrically at 600 K with zero normal stresses on all faces of the simulation box. To mimic the lattice mismatch that is present between BCC-Cu(001) and TiN(001), the simulation box is stretched each timestep according to an engineering strain rate of 10^8 (1/s) along the X and Y directions while the Cauchy stress along the Z direction is kept at zero to mimic the stress relief along the direction normal to the free surface of the film, i.e., Z//BCC[010], as illustrated in Fig. 13(a). The box includes 518,069 Cu atoms with dimensions of $18.619 \times 18.620 \times 18.268$ nm^3 along X//BCC-Cu$\left[\bar{1}01\right]$, Y//BCC-Cu[101], and Z//BCC-Cu[010], respectively. It should be noted that XYZ notation is reserved for the undeformed configuration while xyz relates to the deformed one.

Fig. 13(a) to (d) and Movie 6(a) display the complete transformation of BCC-Cu to nanotwinned FCC-Cu where the twin boundaries are uniformly separated by a distance of ~3.2 nm. Movie 6(b) shows the same series of snapshots where the BCC-Cu atoms have been filtered out to better track the formation of the FCC-Cu phase. As it can be seen from Movie 6(b), no defect nucleates in the vicinity of the void, and FCC-Cu nuclei arise throughout the system. Afterward, these nuclei grow and coalesce in block-like regions such that they are uniformly distributed in the XY or xy plane of the simulation or the plane normal to Z//BCC-Cu[010] or z//FCC-Cu[110] direction. The FCC blocks continue to thicken until their boundaries meet with each other, and twin boundaries with HCP structure are formed.

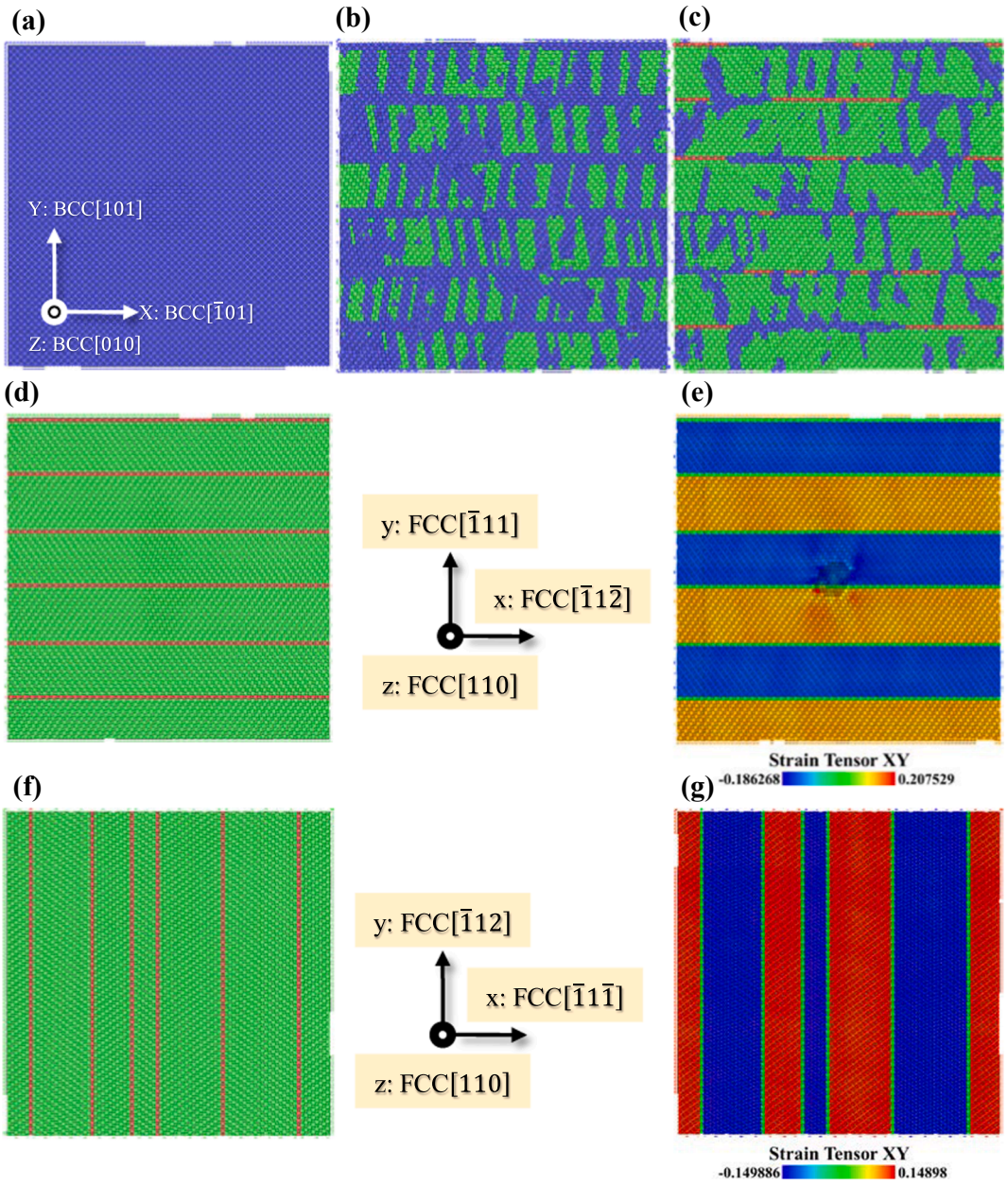

Fig. 13. **(a)** Fully periodic MD simulation box containing a BCC-Cu crystal that contains a spherical void of 2 nm in diameter located at the center of the simulation box. The box is deformed by stretching it in the xy-plane according to an engineering strain rate of 10^8 (1/s) along X (or x) and Y (or y) directions while the Cauchy stress along Z (or z) is kept zero at the simulation temperature of 600 K. **(b)**, **(c)**, and **(d)** Sequence of snapshots depicting the transformation of BCC-Cu to nanotwinned FCC-Cu in which the atoms are colored according to ICNA: blue means BCC, red relates to HCP, green pertains to FCC, and white is assigned to atoms with unidentified structure. Twin boundaries have HCP structure. **(e)** Map of the shear strain ε_{XY} per atom. **(f)** FCC-Cu with nonuniformly and 90° rotated distributed twin boundaries transformed from the same BCC-Cu as in (a) but in the absence of the void. **(g)** Map of shear strain ε_{XY} per atom related to the box with no void.

This block-formation of FCC-Cu within the BCC-Cu is indeed driven by significant localization of shear strain ε_{XY}, as shown in Fig. 13(e) and Movies 6(c) and 6(d). In Movie 6(c), the atoms are colored according to their net atomic displacements along X//BCC-Cu$\left[\bar{1}01\right]$ or x//FCC-Cu$\left[\bar{1}\bar{1}2\right]$ with respect to the undeformed BCC-Cu configuration, since this displacement component contributes the most to the displacements of atoms in the whole process. Also, it should be noted that only the internal (non-affine) displacements of the particles are retained after eliminating the homogeneous computational cell deformation. Movie 6(c) illustrates that by straining the box, layers of BCC-Cu atoms corresponding to the locations of twin boundaries in the FCC-Cu are substantially displaced along X//BCC-Cu$\left[\bar{1}01\right]$ or x//FCC-Cu$\left[\bar{1}\bar{1}2\right]$. Accordingly, as shown in Movie 6(d), alternating patches of localized shear strain ε_{XY} in the form of shear bands start to develop along Z//BCC-Cu[010] or z//FCC-Cu[110] direction. Then, as it can be seen from Fig. 13(e) and Movie 6(d), these shear bands are fully developed in the regions between the locations of the twin boundaries. Subsequently, to reduce the significant increase in the strain energy due to notably localized shear in these regions, the martensitic transformation of BCC-Cu to nanotwinned FCC-Cu phase occurs, as shown in Fig. 13(d), Movie 6(a), and Movie 6(b).

It should be noted that in the whole process of BCC-Cu to nanotwinned FCC-Cu transformation, the void was surrounded by the FCC regions, and the twin boundary wrapped around the void without showing any distortion in its structure, as shown in Movies 6(b) and 7. Since the void did not appear to be necessary for the transformation, the

same simulation box above with no void was strained in the same directions with the same strain rate magnitudes in X and Y directions. The transformation of BCC-Cu to nanotwinned FCC-Cu due to localized shear strain ε_{XY} can be seen in Fig. 13(f) and (g) and Movie 8. The sample with no void undergoes the same martensitic transformation of BCC-to-FCC Cu with the main differences described as follows. The twins are generated with non-uniform thicknesses in Fig. 13(f), and the twin boundaries in Fig. 13(f) are rotated 90° with respect to the ones in the sample with void in Fig. 13(d). The transformation in Fig. 13(f) confirms that the presence of defects, such as the nanovoid, have little effect on the martensitic BCC-to-FCC transformation except in terms of the distribution and inclination of twin boundaries. Therefore, it is reasonable to consider that in different regions of the Cu thin film, where a variety of defects can be present on the TiN substrate or generated in the thin film during the growth of the Cu thin film, one should see regions with differently oriented twins similar to the ones found in the experimental observations in Fig. 4. In fact, during deposition, when the Cu thin film grows to a sufficient thickness, the effect of the interface and free surface on the center of the film becomes weaker than the effect of strain energy differences between BCC- and FCC-Cu phases, and consequently, the nanotwinned FCC-Cu will form as shown in Fig. 6(d), Movie 2(a), and Fig. 7.

To elaborate further on the martensitic transformation in Fig. 13(a) to (d), the kinematics associated with this transformation can be found in Fig. 14 and Movie 6(c). Twin boundaries have been marked by white dashed lines in Fig. 14(a), and they are normal to BCC-Cu[101] or FCC-Cu$\left[\bar{1}11\right]$ direction. As it can be seen from Fig. 14(a) and Movie 6(c), the atoms that are located at the twin boundaries have been significantly moved along the X//BCC-Cu$\left[\bar{1}01\right]$ or x//FCC-Cu$\left[\bar{1}1\bar{2}\right]$ direction. More details can be found in Fig. 14(b) where the arrows indicate the atomic displacements related to the atoms located inside the white frame in Fig. 14(a), and the arrows have been colored based on their displacement magnitudes along X//BCC-Cu$\left[\bar{1}01\right]$ or x//FCC-Cu$\left[\bar{1}1\bar{2}\right]$ direction. In Fig. 14(b), the X//BCC-Cu$\left[\bar{1}01\right]$ or x//FCC-Cu$\left[\bar{1}1\bar{2}\right]$ displacements in the regions between the twin boundaries decrease, then become zero, and increase linearly again along Y//BCC-Cu[101] or y//FCC-Cu$\left[\bar{1}11\right]$ direction. Accordingly, as shown in Fig. 14(b), one can recognize an invariant plane in which the displacement profile becomes zero. The schematic associated with this invariant plane in BCC-to-FCC Cu transformation is similar but in reverse to the one depicting an FCC-to-BCC transformation, in Fig. 14(c) following [69].

It is evident from Figs. 13 and 14 and Movies 6 and 8 that simple shearing [70] prevails during BCC-to-FCC Cu transformation on BCC-Cu{110} or FCC-Cu{111} planes, and maximum shearing is localized at twin boundaries. It is worth mentioning that the BCC-to-FCC Cu phase transformation revealed in Figs. 13, 14(a), and (b) and in Movies 6 and 8 is exactly the reverse of the transformation with the same deformation mechanism that Karewar et al. [69] found in their MD simulation of cooling a pure Fe with nanotwinned FCC structure where twin boundaries are parallel to each other. The schematic in Fig. 14(c) following [69] depicts the FCC-to-BCC iron transformation with the invariant plane. This mechanism is similar but in reverse to the one in the BCC-to-FCC Cu transformation. In fact, they observed in their MD simulation

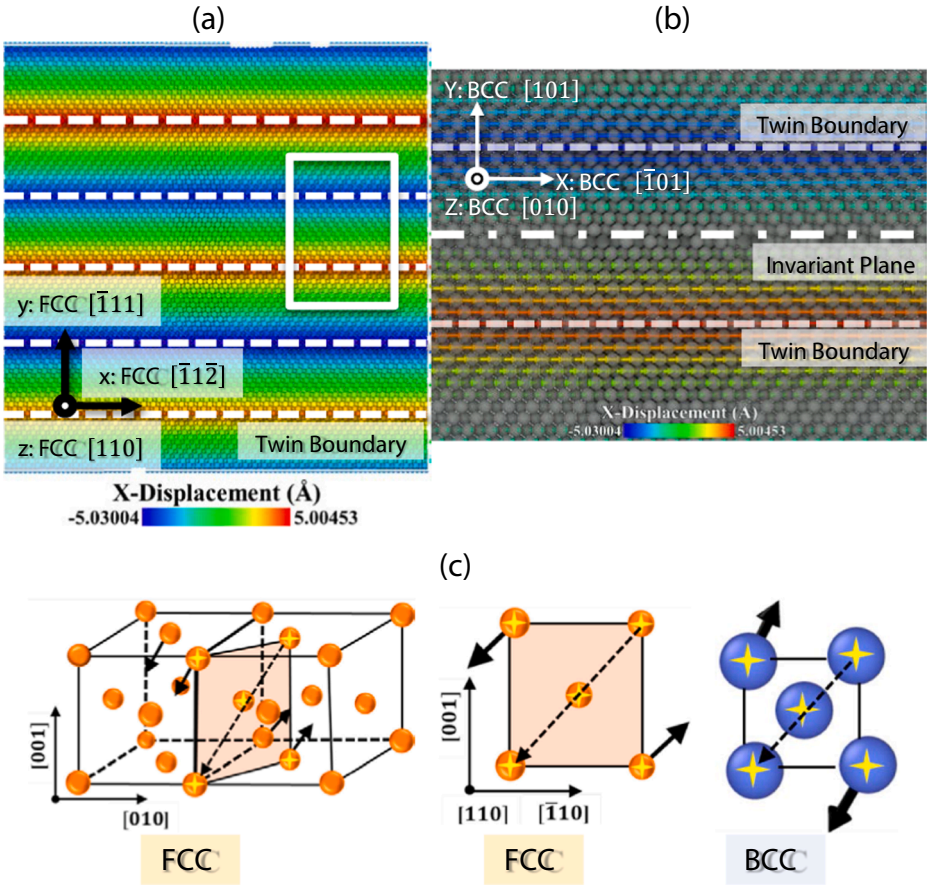

Fig. 14. **(a)** Atoms are colored according to their net atomic displacements along X//BCC-Cu$\left[\bar{1}01\right]$ or x//FCC-Cu$\left[\bar{1}1\bar{2}\right]$ direction only, and twin boundaries have been marked by white dashed lines. **(b)** Magnified region from inside the white frame in (a) with the arrows colored according to their net atomic displacements along X//BCC-Cu$\left[\bar{1}01\right]$ or x//FCC-Cu$\left[\bar{1}1\bar{2}\right]$ direction only. The dashed-dotted white line indicates the location of the invariant plane. **(c)** Schematic of (b) taken from [70].

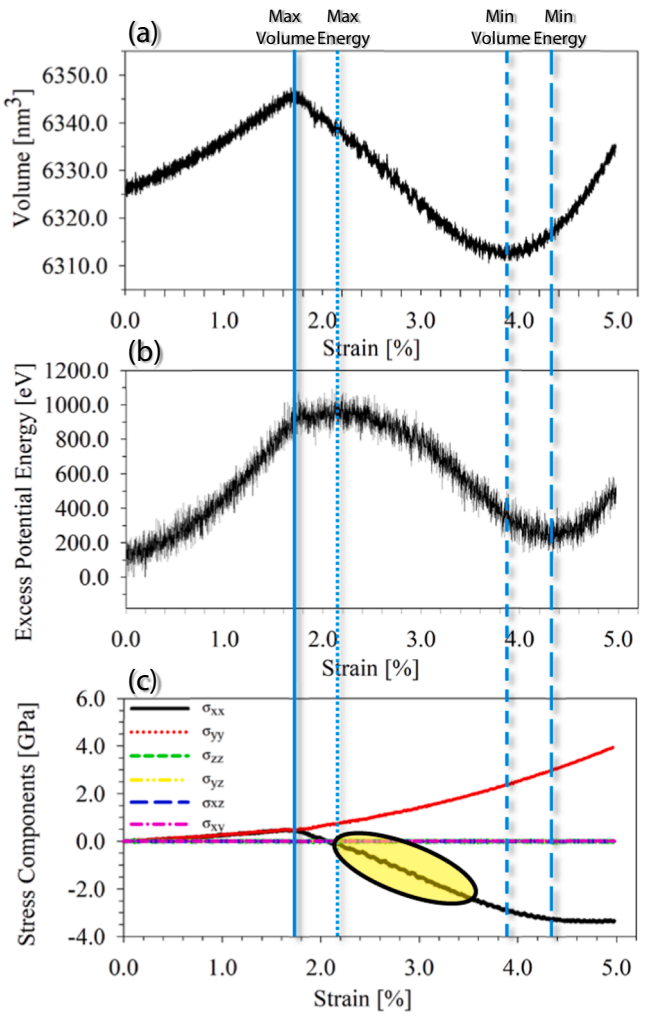

Fig. 15. **(a)** Change in the volume of the MD simulation box during straining of a BCC-Cu crystal versus in-plane engineering strain **(b)** Variation of the excess potential energy relative to the configuration with the lowest potential energy in the entire simulation. **(c)** Profiles of the variation of the six stress components during straining. The transparent yellow oval indicates portion of σ_{xx} profile with serrated character.

that the nanotwinned FCC-Fe is sheared notably on twin boundaries to transform the FCC-Fe to BCC-Fe with the reverse of the kinematics shown in Fig. 14(a) or (b).

To gain more insights into the BCC-to-FCC Cu transformation, Fig. 15 presents the change of volume, excess potential energy, and stress components versus in-plane strain magnitude for the sample with the nanovoid in Fig. 13. The sample with no void had very similar trends, except that the trends associated with σ_{xx} and σ_{yy} stress components should be switched, so the data for the sample without a void are not shown. As it can be seen from Fig. 15(a), by increasing in-plane strain magnitude, the BCC-Cu system expands to a maximum volume at the strain of ~1.7% where the atoms are stimulated to be displaced in a cooperative fashion in opposite directions along X//BCC-Cu $\left[\bar{1}01\right]$ or x// FCC-Cu $\left[\bar{1}1\bar{2}\right]$ direction (see Fig. 14(a) and Movie 6(c)). Then, the system volume shrinks due to development of simple shearing and subsequent formation of FCC blocks after reaching the peak in the energy profile at the strain of ~2.1% in Fig. 15(b) (see Movie 6(b) for more details). Regarding the orientation relationship in Eq. (4), the whole process described here is indeed the Nishiyama-Wasserman mechanism [71,72] in which the change of the crystal structure during the BCC-to-FCC Cu phase transformation occurs through shearing and is followed by the expansion or contraction of the lattice to achieve the correct atomic density. It should be noted that after overcoming the energy barrier at the strain of ~2.1% in Fig. 15(b) and going through a minimum in volume at the strain of ~3.8% in Fig. 15(a), the system needs to expand its volume again to reach the configuration with the lowest potential energy at the strain of ~4.3% in Fig. 15(b).

The BCC-to-FCC Cu transformation by the Nishiyama-Wasserman mechanism originates from shear instability related to BCC-Cu{110} planes [73]. In fact, it can be observed from Table S1 in Supplementary Information that the BCC-Cu elastic constant or shear modulus C_{55} has a value of ~3 GPa, which is notably lower than its FCC-Cu counterpart, i.e., ~81 GPa. This shear instability can also be identified in the stress profiles shown in Fig. 15(c) which shows the variation of the six different stress components against the percent change of in-plane engineering strain. Consistent with the in-plane strain condition, only σ_{xx} and σ_{yy} stress components are nonzero through the entire simulation, and both σ_{xx} and σ_{yy} stress components are increasing with the same rate up to the point corresponding to the maximum volume at the strain of ~1.7% in Fig. 15(a). After this point, however, σ_{yy} continues to increase with a higher rate while σ_{xx} decreases until it becomes zero which corresponds roughly to the maximum value in the excess potential energy profile at the strain of ~2.1% in Fig. 15(b). This drop is indeed related to initiation of the shear instability in the material when atoms begin to be displaced in a cooperative fashion in opposite directions along X//BCC-Cu $\left[\bar{1}01\right]$ or x//FCC-Cu $\left[\bar{1}1\bar{2}\right]$ direction (more details can be seen in Movie 6). Meanwhile, due to the increased rate of change in the profile of σ_{yy}, the material is stretched at a higher rate in this direction, i.e., Y// BCC-Cu[101] or y//FCC-Cu $\left[\bar{1}11\right]$ direction, causing the system to experience notable shrinkage along X//BCC-Cu $\left[\bar{1}01\right]$ or x//FCC-Cu $\left[\bar{1}1\bar{2}\right]$ direction. After a while, σ_{xx} becomes compressive, and in the compression part of σ_{xx} profile in Fig. 15(c), one can identify a serrated stress profile, which has been marked by a transparent yellow oval. This serration is indeed indicative of successive shear yielding while FCC blocks are formed (see Movies 6(b), 6(c), and (6d)).

5. Summary

Simulations performed in this work was motivated by experimental observations made in UHV dc magnetron sputter deposition of Cu on TiN(001) at low temperatures, especially the observation of a new orientation relationship of Cu(110)//TiN(001), the OR_B as described in this paper. The simulation work therefore focused on revealing atomistic details of the growth mechanisms operating during Cu thin film deposition on TiN substrates by employing a physics-based MD/tfMC simulation methodology. The simulations dealt with Cu growth on TiN in the two most common orientations, i.e., TiN(001) and TiN(111). A sequential MD/tfMC algorithm was devised and applied to simulate the processes involved in deposition of Cu films at 600 K on TiN(001), N-terminated TiN(111), and Ti-terminated TiN(111) substrates, the results of which were compared against experimental observations of Cu growth on TiN(001) by the present authors as well as ⟨111⟩ direction growth reported in the literature.

It was revealed that 3D Cu islands nucleate randomly on TiN(001). Further deposition and island coalescence lead to growth of the islands primarily in the lateral direction and developing nearly 2D islands. Eventually, a continuous Cu thin film grew in the BCC phase. However, after the film increased further in thickness, the Cu film underwent a structural transformation, transforming the BCC crystal structure to a nanotwinned FCC one. The BCC-to-FCC Cu structural transformation was examined via additional MD simulations, and it was demonstrated that, due to the shear instability of BCC-Cu{110} planes, BCC-Cu transforms martensitically to nanotwinned FCC-Cu, such that the maximum shearing is localized at the twin boundaries parallel to BCC-Cu{110} or FCC-

Cu{111} palnes. Consequently, an invariant plane was identified where no shearing occurs, and it is located in the middle of the regions between twin boundaries. This simple shear mechanism was accompanied by contraction of the lattice to achieve the correct atomic density such that the whole process was recognized to occur through the Nishiyama-Wasserman mechanism.

Simulation of the deposition on the N-terminated TiN(111) substrate showed that the film microstructure is controlled by the poor Cu wettability of the TiN substrate. Therefore, during deposition, 3D islands were developed via different mechanisms such as: notable diffusion of Cu adatoms and subsequent growth of 3D islands from aggregation of these adatoms, coalescence of small islands, facet migration among large FCC-Cu islands, and nucleation and growth of 2D layers on Cu{100} and Cu{111} facets which were located on the surfaces of the large islands. Moreover, formation of large and tall 3D islands resulted in shadowing instability due to interception of the flux of incoming Cu species more often. Therefore, Cu deposition on weakly interacting N-rich TiN substrates may not result in continuous thin films, and it is possible for the deposited material to develop notable porosity during growth.

In contrast to N-terminated TiN(111) substrate, at the early stage of growth, deposited Cu on Ti-terminated TiN(111) completely wetted the TiN surface. Subsequently, 2D patches nucleated and grew on top of the already deposited Cu layers. However, after forming a 2-layer-thick nanotwin close to the Cu/TiN interface, surface diffusion from the upper layers down the steps going toward the TiN substrate was hindered due to a Schwoebel instability. Therefore, Cu growth was biased toward the direction normal to the TiN(111) substrate instead of the lateral directions because of nucleating new layers on top of the islands and slow downhill diffusion. Moreover, due to the orientation relationship of FCC-Cu[111]//TiN[111], FCC-Cu $\left[1\bar{1}0\right]$//TiN $\left[1\bar{1}0\right]$, and FCC-Cu $\left[\bar{1}\bar{1}2\right]$//TiN $\left[\bar{1}\bar{1}2\right]$, the misfit strain of 14.3% at 600 K between Cu and TiN was accommodated by formation of a MDN at the Cu(111)//Ti-terminated TiN(111) interface. The MDN was composed of straight dislocations with pure edge character aligned with ⟨110⟩ directions and $(a_{Cu}/6)\langle 112\rangle$ Burgers vectors, forming Shockley partials connected by smeared nodes. Also, the entire MDN could be translated in a rigid manner in different directions due to a low shear strength of the Cu(111)/Ti-terminated TiN(111) interface, originating from minimal pinning offered by nodes of the MDN and having an isotropic in-plane plastic response resulting from 3-fold symmetry of the MDN structure.

The present simulation results provide deep insights into some complexities of the growth mechanisms operating during Cu growth on TiN and shed light on related thin film growth in weakly-interacting metal/substrate systems.

CRediT authorship contribution statement

Reza Namakian: Conceptualization, Methodology, Software, Validation, Formal analysis, Investigation, Data curation, Writing – original draft, Visualization. **Brian R. Novak:** Conceptualization, Methodology, Software, Validation, Formal analysis, Investigation, Data curation, Writing – review & editing, Visualization, Supervision. **Xiaoman Zhang:** Conceptualization, Formal analysis, Data curation, Writing – review & editing, Visualization. **Wen Jin Meng:** Conceptualization, Validation, Investigation, Resources, Data curation, Writing – review & editing, Supervision, Project administration, Funding acquisition. **Dorel Moldovan:** Conceptualization, Validation, Investigation, Resources, Data curation, Writing – review & editing, Supervision, Project administration, Funding acquisition.

Declaration of Competing Interest

The authors declare that they have no known competing financial interests or personal relationships that could have appeared to influence the work reported in this paper.

Acknowledgments

The authors are grateful to Drs. Kristof Bal, Pablo Piaggi, Thomas Swinburne, Abu Shama M. Miraz, and Collin D. Wick for their invaluable discussions on this subject. Portions of this research were conducted with high-performance computational resources provided by Louisiana State University (http://www.hpc.lsu.edu) and the Louisiana Optical Network Infrastructure (http://www.loni.org). This work was funded in part by the NSF EPSCoR program, awards OIA-1541079 and OIA-1946231. Use of experimental facilities at the LSU Shared Instrumentation Facility (SIF), a part of the Louisiana Core User Facilities (CUF), is acknowledged.

Appendix A. Supplementary material

Supplementary data to this article can be found online at https://doi.org/10.1016/j.apsusc.2021.151013.

References

[1] N. Setter, D. Damjanovic, L. Eng, G. Fox, S. Gevorgian, S. Hong, A. Kingon, H. Kohlstedt, N.Y. Park, G.B. Stephenson, I. Stolitchnov, A.K. Taganstev, D. V. Taylor, T. Yamada, S. Streiffer, Ferroelectric thin films: Review of materials, properties, and applications (vol 100, art no 051606, 2006), J. Appl. Phys. 100 (2006).
[2] F. Tietz, P. Nikolopoulos, Metal/Ceramic Interface Properties and Their Effects on SOFC Development, Fuel Cells 9 (2009) 867–872.
[3] R. Polanco, A. De Pablos, P. Miranzo, M.I. Osendi, Metal-ceramic interfaces: joining silicon nitride-stainless steel, Appl. Surf. Sci. 238 (2004) 506–512.
[4] R. Darolia, Thermal barrier coatings technology: Critical review, progress update, remaining challenges and prospects, Int. Mater. Rev. 58 (2013) 315–348.
[5] J.Y. Tsao, J.P. Harbison, Materials Fundamentals of Molecular Beam Epitaxy, Phys. Today 46 (1993) 125–126.
[6] T. Itoh, Ion Beam Assisted Film Growth, Elsevier, 1989.
[7] L.E. Toth, Transition metal carbides and nitrides, Academic Press, New York and London, 1971.
[8] B.X. Dong, H.Y. Yang, F. Qiu, Q. Li, S.L. Shu, B.Q. Zhang, Q.C. Jiang, Design of TiCx nanoparticles and their morphology manipulating mechanisms by stoichiometric ratios: Experiment and first-principle calculation, Mater. Des. 181 (2019).
[9] G.V. Naik, B. Saha, J. Liu, S.M. Saber, E.A. Stach, J.M.K. Irudayaraj, T.D. Sands, V. M. Shalaev, A. Boltasseva, Epitaxial superlattices with titanium nitride as a plasmonic component for optical hyperbolic metamaterials, PNAS 111 (2014) 7546–7551.
[10] M. Braic, N.C. Zoita, M. Danila, C.E.A. Grigorescu, C. Logofatu, Hetero-epitaxial growth of TiC films on MgO(001) at 100 degrees C by DC reactive magnetron sputtering, Thin Solid Films 589 (2015) 590–596.
[11] B.W. Karr, I. Petrov, D.G. Cahill, J.E. Greene, Morphology of epitaxial TiN(001) grown by magnetron sputtering, Appl. Phys. Lett. 70 (1997) 1703–1705.
[12] S.B. Sinnott, E.C. Dickey, Ceramic/metal interface structures and their relationship to atomic- and meso-scale properties, Mater. Sci. Eng. R-Rep. 43 (2003) 1–59.
[13] S. Cazottes, Z.L. Zhang, R. Daniel, J.S. Chawla, D. Gall, G. Dehm, Structural characterization of a Cu/MgO(001) interface using C-S-corrected HRTEM, Thin Solid Films 519 (2010) 1662–1667.
[14] Z.L. Zhang, Y. Long, S. Cazottes, R. Daniel, C. Mitterer, G. Dehm, The peculiarity of the metal-ceramic interface, Sci. Rep. 5 (2015).
[15] J.S. Chawla, X.Y. Zhang, D. Gall, Epitaxial TiN(001) wetting layer for growth of thin single-crystal Cu(001), in: Journal of Applied Physics, American Institute of PhysicsAIP, 2011, p. 043714.
[16] X.M. Zhang, S. Shao, A.S.M. Miraz, C.D. Wick, B.R. Ramachandran, W.J. Meng, Low temperature growth of Cu thin films on TiN(001) templates: Structure and energetics, Materialia 12 (2020) 100748.
[17] G.Y. Yang, Y. Liu, Z.Q. Hang, N.Y. Xi, H. Fu, H. Chen, Adhesion at cerium doped metal-ceramic alpha-Fe/WC interface: A first-principles calculation, J. Rare Earths 37 (2019) 773–780.
[18] F.Y. Lin, A. Chernatynskiy, J.C. Nino, J.L. Jones, R. Hennig, S.B. Sinnott, Role of composition and structure on the properties of metal/multifunctional ceramic interfaces, J. Appl. Phys. 120 (2016).

[19] X. Zhang, B. Zhang, Y. Mu, S. Shao, C.D. Wick, B.R. Ramachandran, W.J. Meng, Mechanical failure of metal/ceramic interfacial regions under shear loading, in: Acta Materialia, Acta Materialia Inc, 2017, pp. 224–236.
[20] X.Y. Guo, Y. Zhang, Y.G. Jung, L. Li, J. Knapp, J. Zhang, Ideal tensile strength and shear strength of ZrO2(111)/Ni(111) ceramic-metal Interface: A first principle study, Mater. Des. 112 (2016) 254–262.
[21] A. Sazgar, M.R. Movahhedy, M. Mahnama, S. Sohrabpour, A molecular dynamics study of bond strength and interface conditions in the Al/Al2O3 metal-ceramic composites, Comput. Mater. Sci. 109 (2015) 200–208.
[22] A.M. Miraz, S.T. Sun, S. Shao, W.J. Meng, B.R. Ramachandran, C.D. Wick, Computational study of metal/ceramic interfacial adhesion and barriers to shear displacement, Comput. Mater. Sci. 168 (2019) 104–115.
[23] A.S.M. Miraz, N. Dhariwal, W.J. Meng, B.R. Ramachandran, C.D. Wick, Development and application of interatomic potentials to study the stability and shear strength of Ti/TiN and Cu/TiN interfaces, in: Materials and Design, Elsevier Ltd, 2020, p. 109123.
[24] E.C. Neyts, A. Bogaerts, Combining molecular dynamics with Monte Carlo simulations: implementations and applications, Theor. Chem. Acc. 132 (2013) 12.
[25] E.C. Neyts, P. Brault, Molecular Dynamics Simulations for Plasma-Surface Interactions, in: Plasma Processes and Polymers, Wiley-VCH Verlag, 2017, pp. 1600145.
[26] K.M. Bal, E.C. Neyts, On the time scale associated with Monte Carlo simulations, J. Chem. Phys. 141 (2014), 204104.
[27] E. Braun, J. Gilmer, H.B. Mayes, D.L. Mobley, J.I. Monroe, S. Prasad, D. M. Zuckerman, Best Practices for Foundations in Molecular Simulations [Article v1.0], in: Living Journal of Computational Molecular Science, University of Colorado at Boulder, 2019, p. 5957.
[28] M. Timonova, J. Groenewegen, B.J. Thijsse, Modeling diffusion and phase transitions by a uniform-acceptance force-bias Monte Carlo method, in: Physical Review B - Condensed Matter and Materials Physics, American Physical Society, 2010, p. 144107.
[29] M.J. Mees, G. Pourtois, E.C. Neyts, B.J. Thijsse, A. Stesmans, Uniform-acceptance force-bias Monte Carlo method with time scale to study solid-state diffusion. Physical Review B - Condensed Matter and Materials Physics, American Physical Society, 2012.
[30] B. Lü, G.A. Almyras, V. Gervilla, J.E. Greene, K. Sarakinos, Formation and morphological evolution of self-similar 3D nanostructures on weakly interacting substrates. Physical Review Materials, American Physical Society, 2018.
[31] V. Gervilla, G.A. Almyras, F. Thunström, J.E. Greene, K. Sarakinos, Dynamics of 3D-island growth on weakly-interacting substrates, in: Applied Surface Science, Elsevier B.V., 2019, pp. 383–390.
[32] V. Gervilla, G.A. Almyras, B. Lü, K. Sarakinos, Coalescence dynamics of 3D islands on weakly-interacting substrates, in: Scientific Reports, Nature Research, 2020, pp. 1–8.
[33] D. Zhang, L. Peng, X. Li, P. Yi, X. Lai, Controlling the Nucleation and Growth Orientation of Nanocrystalline Carbon Films during Plasma-Assisted Deposition: A Reactive Molecular Dynamics/Monte Carlo Study, in: Journal of the American Chemical Society, American Chemical Society, 2020, pp. 2617–2627.
[34] S. Plimpton, Fast parallel algorithms for short-range molecular dynamics, in: Journal of Computational Physics, Academic Press, 1995, pp. 1–19.
[35] P. Hirel, Atomsk: A tool for manipulating and converting atomic data files, in: Computer Physics Communications, North-Holland, 2015, pp. 212–219.
[36] J. Guénolé, W.G. Nöhring, A. Vaid, F. Houllé, Z. Xie, A. Prakash, E. Bitzek, Assessment and optimization of the fast inertial relaxation engine (FIRE) for energy minimization in atomistic simulations and its implementation in LAMMPS. Computational Materials Science, Elsevier B.V., 2020.
[37] T. Schneider, E. Stoll, Molecular-dynamics study of a three-dimensional one-component model for distortive phase transitions, in: Physical Review B, American Physical Society, 1978, pp. 1302–1322.
[38] N. Grønbech-Jensen, Complete set of stochastic Verlet-type thermostats for correct Langevin simulations. Molecular Physics, Taylor and Francis Ltd., 2020.
[39] M. Parrinello, A. Rahman, Polymorphic transitions in single crystals: A new molecular dynamics method, in: Journal of Applied Physics, American Institute of PhysicsAIP, 1981, pp. 7182–7190.
[40] G.J. Martyna, D.J. Tobias, M.L. Klein, Constant pressure molecular dynamics algorithms, in: The Journal of Chemical Physics, American Institute of PhysicsAIP, 1994, pp. 4177–4189.
[41] W. Shinoda, M. Shiga, M. Mikami, Rapid estimation of elastic constants by molecular dynamics simulation under constant stress. Physical Review B - Condensed Matter and Materials Physics, American Physical Society, 2004.
[42] M.E. Tuckerman, J. Alejandre, R. López-Rendón, A.L. Jochim, G.J. Martyna, A Liouville-operator derived measure-preserving integrator for molecular dynamics simulations in the isothermal-isobaric ensemble, in: Journal of Physics A: Mathematical and General, IOP Publishing, 2006, pp. 5629–5651.
[43] R.E. Miller, E.B. Tadmor, J.S. Gibson, N. Bernstein, F. Pavia, Molecular dynamics at constant Cauchy stress, in: Journal of Chemical Physics, American Institute of Physics Inc., 2016, pp. 184107.
[44] R. Namakian, G.Z. Voyiadjis, P. Kwaśniak, On the slip and twinning mechanisms on first order pyramidal plane of magnesium: Molecular dynamics simulations and first principal studies, Mater. Des. (2020), 108648.
[45] E. Asadi, M. Asle Zaeem, S. Nouranian, M.I. Baskes, Quantitative modeling of the equilibration of two-phase solid-liquid Fe by atomistic simulations on diffusive time scales. Physical Review B - Condensed Matter and Materials Physics, American Physical Society, 2015.
[46] S. Kavousi, B.R. Novak, M.I. Baskes, M.A. Zaeem, D. Moldovan, Modified embedded-atom method potential for high-temperature crystal-melt properties of Ti-Ni alloys and its application to phase field simulation of solidification, in: Modelling and Simulation in Materials Science and Engineering, Institute of Physics Publishing, 2020, p. 015006.
[47] A. Stukowski, Visualization and analysis of atomistic simulation data with OVITO-the Open Visualization Tool, in: Modelling and Simulation in Materials Science and Engineering, IOP Publishing, 2010, pp. 015012.
[48] P.M. Larsen, Revisiting the Common Neighbour Analysis and the Centrosymmetry Parameter, ArXiv. (2020) http://arxiv.org/abs/2003.08879, (2021).
[49] A.M. Hodge, Y.M. Wang, T.W. Barbee, Mechanical deformation of high-purity sputter-deposited nano-twinned copper, in: Scripta Materialia, Pergamon, 2008, pp. 163–166.
[50] K. Abe, Y. Harada, H. Onoda, Cu crystallographic texture control in Cu/refractory-metal layered structure as interconnects, in: Appl. Phys. Lett., American Institute of Physics Inc., 1997, pp. 2782–2784.
[51] A. Kvit, A.K. Sharma, J. Narayan, Growth of epitaxial Cu/TiN/6H-SiC(0001) heterostructures by pulsed laser deposition, in: Materials Research Society Symposium - Proceedings, Materials Research Society, 2000, pp. 159–163.
[52] G. Szwachta, M. Gajewska, P. Dłużewski, S. Kąc, M. Przybylski, Characterization of MgO/TiN bilayer deposited on cube-textured copper using pulsed-laser deposition technique. Thin Solid Films, Elsevier B.V., 2019.
[53] K. Abe, Y. Harada, H. Onoda, Study of crystal orientation in Cu film on TiN layered structures, in: Journal of Vacuum Science & Technology B: Microelectronics and Nanometer Structures, American Vacuum Society, 1999, p. 1464.
[54] M. Mühlbacher, A.S. Bochkarev, F. Mendez-Martin, B. Sartory, L. Chitu, M.N. Popov, P. Puschnig, J. Spitaler, H. Ding, N. Schalk, J. Lu, L. Hultman, C. Mitterer, Cu diffusion in single-crystal and polycrystalline TiN barrier layers: A high-resolution experimental study supported by first-principles calculations, in: Journal of Applied Physics, American Institute of Physics Inc., 2015, pp. 085307.
[55] S. Zhang, F. Yan, Y. Yang, M. Yan, Y. Zhang, J. Guo, H. Li, Effects of sputtering gas on microstructure and tribological properties of titanium nitride films, in: Applied Surface Science, Elsevier B.V, 2019, pp. 61–69.
[56] M. Mühlbacher, G. Greczynski, B. Sartory, N. Schalk, J. Lu, I. Petrov, J.E. Greene, L. Hultman, C. Mitterer, Enhanced Ti0.84Ta0.16N diffusion barriers, grown by a hybrid sputtering technique with no substrate heating, between Si(001) wafers and Cu overlayers, in: Scientific Reports, Nature Publishing Group, 2018, pp. 1–9.
[57] Y.-B. Park, Growth and fractal scaling nature of copper thin films on TiN surface by metal organic chemical vapor deposition from hexafluoroacethylacetonate Cu[sup (I)] vinyltrimethylsilane, in: Journal of Vacuum Science & Technology B: Microelectronics and Nanometer Structures, American Vacuum Society, 1997, p. 1995.
[58] X. Bai, J. Li, L. Zhu, Structure and properties of TiSiN/Cu multilayer coatings deposited on Ti6Al4V prepared by arc ion plating, in: Surface and Coatings Technology, Elsevier B.V, 2019, pp. 16–25.
[59] R. Kröger, M. Eizenberg, E. Rabkin, D. Cong, L. Chen, The role of kinetics in the nucleation and void formation in copper films produced by chemical vapor deposition, in: Journal of Applied Physics, American Institute of Physics Inc., 2000, pp. 1867–1872.
[60] W. Pan, D.R. Evans, R. Barrowcliff, S.T. Hsu, The growth kinetics study of CVD Cu on TiN barriers, in: Journal De Physique. IV: JP, EDP Sciences, 2001, pp. Pr3-23-Pr23-30.
[61] L. Magagnin, A. Vicenzo, M. Bain, H.W. Toh, H.S. Gamble, P.L. Cavallotti, Nucleation and growth of ECD Cu on PVD TiN from low acid sulfate electrolyte, in: Microelectronic Engineering, Elsevier, 2004, pp. 131–136.
[62] C.L. Chang, C.L. Lin, M.C. Chen, Effect of TiN substrate plasma treatment on copper chemical vapor deposition, in: Japanese Journal of Applied Physics, Part 1: Regular Papers and Short Notes and Review Papers, Japan Society of Applied Physics, 2004, pp. 2442-2446.
[63] L.A. Zepeda-Ruiz, G.H. Gilmer, Monte Carlo Simulations of Crystal Growth, in: Handbook of Crystal Growth: Second Edition, Elsevier Inc., 2015, pp. 445-475.
[64] S. Shao, J. Wang, Relaxation, Structure, and Properties of Semicoherent Interfaces, in: Jom, Minerals, Metals and Materials Society, 2016, pp. 242-252.
[65] D.G. Sangiovanni, Copper adatom, admolecule transport, and island nucleation on TiN(0 0 1) via ab initio molecular dynamics, in: Applied Surface Science, Elsevier B.V, 2018, pp. 180–189.
[66] J. Wang, R.G. Hoagland, A. Misra, Phase transition and dislocation nucleation in Cu-Nb layered composites during physical vapor deposition, in: Journal of Materials Research, Cambridge University Press, 2008, pp. 1009-1014.
[67] S.K. Yadav, R. Ramprasad, J. Wang, A. Misra, X.Y. Liu, First-principles study of Cu/TiN and Al/TiN interfaces: Weak versus strong interfaces, in: Modelling and Simulation in Materials Science and Engineering, Institute of Physics Publishing, 2014, p. 035020.
[68] C.D. Barrett, H. El Kadiri, M.A. Tschopp, Breakdown of the Schmid law in homogeneous and heterogeneous nucleation events of slip and twinning in magnesium, in: Journal of the Mechanics and Physics of Solids, Pergamon, 2012, pp. 2084–2099.
[69] S. Karewar, J. Sietsma, M.J. Santofimia, Effect of pre-existing defects in the parent fcc phase on atomistic mechanisms during the martensitic transformation in pure Fe: A molecular dynamics study, in: Acta Materialia, Acta Materialia Inc, 2018, pp. 71-81.

[70] R. Namakian, G.Z. Voyiadjis, An atomic displacive model for 101¯21¯011 twinning in hexagonal close packed metals with the emphasis on the role of partial stacking faults in formation of {101¯2} twins, in: Acta Materialia, Acta Materialia Inc, 2018, pp. 381-393.
[71] Z. Nishiyama, X-ray investigation of the mechanism of the transformation from face centered cubic lattice to body centered cubic lattice, Sci. Rep. Tohoku Imp Univ. (1934) 637–664.
[72] G. Wassermann, Ueber den Mechanismus der [alpha]-[gamma]-Umwandlung des Eisens, Verlag Stahleisen (1935) 281.
[73] T. Kraft, P.M. Marcus, M. Methfessel, M. Scheffler, Elastic constants of Cu and the instability of its bcc structure, in: Physical Revew B, American Physical Society, 1993, pp. 5886–5890.